

COMBINED GEOPHYSICAL METHODS FOR MAPPING
INFILTRATION PATHWAYS AT THE AURORA WATER AQUIFER
RECHARGE AND RECOVERY SITE

by
Cameron A. Jasper

A thesis submitted to the Faculty and Board of Trustees of the Colorado School of Mines in partial fulfillment of the requirements for the degree of Master of Science in Hydrology.

Golden, Colorado

Date _____

Signed _____

Cameron A. Jasper

Signed _____

Dr. André Revil

Thesis Advisor

Signed _____

Dr. David Benson

Director of the Hydrologic Science and Engineering Program

ABSTRACT

Although aquifer recharge and recovery systems are a sustainable, decentralized, low cost, and low energy approach for the reclamation, treatment, and storage of post-treatment wastewater, they can suffer from poor infiltration rates and the development of a near-surface clogging layer within infiltration ponds. One such aquifer recharge and recovery system, the Aurora Water site in Colorado, U.S.A, functions at about 25% of its predicted capacity to recharge floodplain deposits by flooding infiltration ponds with post-treatment wastewater extracted from river bank aquifers along the South Platte River. The underwater self-potential method was developed to survey self-potential signals at the ground surface in a flooded infiltration pond for mapping infiltration pathways. A method for using heat as a groundwater tracer within the infiltration pond used an array of in situ high-resolution temperature sensing probes. Both relatively positive and negative underwater self-potential anomalies are consistent with observed recovery well pumping rates and specific discharge estimates from temperature data. Results from electrical resistivity tomography and electromagnetics surveys provide consistent electrical conductivity distributions associated with sediment textures. A lab method was developed for resistivity tests of near-surface sediment samples. Forward numerical modeling synthesizes the geophysical information to best match observed self-potential anomalies and provide permeability distributions, which is important for effective aquifer recharge and recovery system design, and optimization strategy development.

TABLE OF CONTENTS

ABSTRACT	iii
LIST OF FIGURES	v
ACKNOWLEDGMENTS	vi
CHAPTER 1 INTRODUCTION	1
1.1 Background	3
1.2 Site Description	7
CHAPTER 2 METHODS	11
2.1 Underwater self-potential	11
2.2 High-resolution temperature sensing	16
2.3 Electrical resistivity tomography	23
2.4 Electromagnetics	26
2.5 Laboratory electrical resistivity tests	27
CHAPTER 3 RESULTS	28
3.1 Underwater self-potential	28
3.2 High-resolution temperature sensing	31
3.3 Electrical resistivity tomography	40
3.4 Electromagnetics	41
3.5 Laboratory electrical resistivity tests	43
3.6 Numerical modeling	46
3.7 Conclusions	48
REFERENCES CITED	49

LIST OF FIGURES

1.10	Sketch of an aquifer recharge and recovery system	3
1.20	The Aurora Water aquifer recharge and recovery site	7
1.21	Algae in the eastern central infiltration pond	9
1.22	Amphibians during wet-cycle operation at the eastern central pond	10
2.10	Relationship between permeability and advected charge density	12
2.11	Numerical COMSOL simulation of self-potential	14
2.12	Sketch of self-potential anomaly	15
2.20	Diagram of the return signal intensity	19
2.21	Calibration workflow in 1DTempPro for running the VS2DH code	20
3.10	Pumping rates during underwater self-potential surveys	29
3.11	Plot of underwater self-potential surveys	30
3.20	Threading epoxy fiberglass rods	32
3.21	Resolution of temperature sensing probes	33
3.22	Top of a recovered high-resolution temperature sensing probe	33
3.23	Bottom of a recovered high-resolution temperature sensing probe	34
3.24	Fujikura arc-fusion splicer	34
3.25	Temperature sensing probe insertion with a backhoe	35
3.26	Thermal conductivity and heat capacity tests	36
3.27	1DTempPro model of probe 1 data	37
3.28	Specific discharge estimates from 1DTempPro	38
3.30	Electrical resistivity tomography survey location	39
3.31	Electrical resistivity tomogram	40
3.40	Electromagnetics (EM-31) survey results	41
3.50	Experimental setup for laboratory resistivity tests	43
3.51	Electrical conductivity maps of laboratory resistivity test results	44
3.60	Simulated 2D vertical cross section location	46
3.61	2D COMSOL groundwater flow simulation	47
3.62	2D COMSOL self-potential simulation	47

ACKNOWLEDGMENTS

I would like to thank the Hydrologic Science and Engineering Program at Colorado School of Mines for granting me this prestigious thesis, and Jörg Drews and Julia Regnery for their support and management of the N.3 project with The Urban Water ERC. I would like to thank André Revil for his ongoing advising, and use of his equipment, Kamini Singha for her guidance and the use of her equipment, and John Selker for his ongoing guidance. This project would not have been possible without funding from the Edna Baily Sussman Foundation and the ongoing assistance and support that Jason Lee, David Begler, and Ted Hartfelder provided at the Aurora Water aquifer recharge and recovery site. I would like to thank Marios Karaoulis, Deqiang Mao, Pauline Kessouri, Jackie Randell, Emily Voytek, Brian Passerella, James Bethune, Emmanuel Padilla, Dan Robinson, Ben Bader, Chris Shaffer, Vincent Alberola, Clinton Meyer, Jonathan Moen, Tristan Acob, Drew Beck, and Katherine Radavich for their assistance in the field, in the lab, and in the machine shop. I would like to thank to my parents, David and Joanie Jasper, as well as Monica Hanson for their encouragement. A particular note of gratitude to John Jezek for his supervision and enduring unconditional help in the Colorado School of Mines machine shop.

CHAPTER 1

INTRODUCTION

The capacity and cost-effectiveness of aquifer recharge and recovery systems is limited by poor infiltration pond hydraulic loading rates and poor recovery well pumping rates (Bouwer & Rice, 1989). Lower, less efficient, recovery well pumping rates can result from both low permeability floodplain deposits and the development of the clogging layer within the near-surface sediments of infiltration ponds (Bouwer & Rice, 1989). The accumulation of inorganic and organic fines induces near-surface clogging, which can dominate the hydraulic loading rate of infiltration ponds over time (Bouwer & Rice, 1989). Restricted near-surface discharge due to clogging layer development results in more stable surface water and enhanced algae growth, which can lead to less favorable anoxic conditions during aquifer recharge and recovery system operation (Ma & Spalding, 1997). Effective system design and optimization strategy development requires the combination of geophysical information for mapping infiltration pathways and estimating near-surface permeability distributions.

The underwater self-potential method is sensitive to streaming current produced by groundwater flow and the advection of excess charges within electrical double layers around negatively charged surfaces (Ikard *et al.*, 2012). Self-potential signals are affected by differences in sediment textures, permeability, discharge rates, and electrical conductivity. Relatively negative self-potential anomalies arise from streaming current contributions associated with infiltration, higher permeability, and lower electrical conductivity, while relatively positive self-potential anomalies are associated with less

infiltration, lower permeability, and increased electrical conductivity. It is advantageous to combine several geophysical methods for prior information of specific discharge and electrical conductivity in order to estimate permeability based on observed self-potential anomalies. High-resolution temperature sensing can be used to estimate specific discharge by using heat as a groundwater tracer (Briggs *et al.*, 2012). Electrical resistivity tomography is capable of imaging subsurface electrical properties, sensitive to saturation, dissolved solids, and sediment textures (Revil *et al.*, 2012). Electromagnetics methods are utilized for estimating electrical conductivity at a half-depth, where quadrature signals of electromagnetic radiation are associated with saturation, dissolved solids, and sediment textures (Morris, 2009). Laboratory electrical resistivity tests of sediment samples can be accomplished with an impedance spectrometry system (Zimmermann *et al.*, 2008). Increased organic and inorganic fines content within saturated sediments results in increased electrical conductivity, increased excess charge within porewater, and decreased permeability.

The synthesis of information from these geophysical methods can be achieved with finite element forward modeling in COMSOL Multiphysics. Electrical conductivity and permeability can be spatially discretized to best match the observed relative underwater self-potential anomalies. The forward simulation of self-potential anomalies starts with applying electrical conductivities to different distributed finite element layers, by combining information from electrical resistivity tomography, electromagnetics, and laboratory electrical resistivity tests. Permeability parameters are constrained by near-surface specific discharge estimates from high-resolution temperature sensing. Solving for the relative self-potential anomalies with the coupled electrical continuity equation

requires the prior permeability, groundwater velocity, and electrical conductivity distributions. In order to best match the observed positive or negative self-potential anomalies, permeability distributions and magnitudes are calibrated within different layers and prior constrains. This forward modeling process allows for the combination of geophysical methods in order to estimate near-surface permeability distributions, the locations of primary infiltration pathways and areas with restricted near-surface discharge due to clogging.

1.1 Background

Aquifer recharge and recovery systems are a sustainable, decentralized, low cost, and low energy approach for the reclamation, treatment, and storage of post-treatment wastewater (Hering *et al.*, 2013). These systems utilize biodegradation, sorption, and storage capacities of unconfined aquifers to improve water quality, offer wetland habitat, and increase long-term average rates of groundwater abstraction in response to water deficits (Hering *et al.*, 2013). The successful operation of aquifer recharge and recovery systems relies on recharging groundwater through the use of infiltration ponds (Figure 1.10).

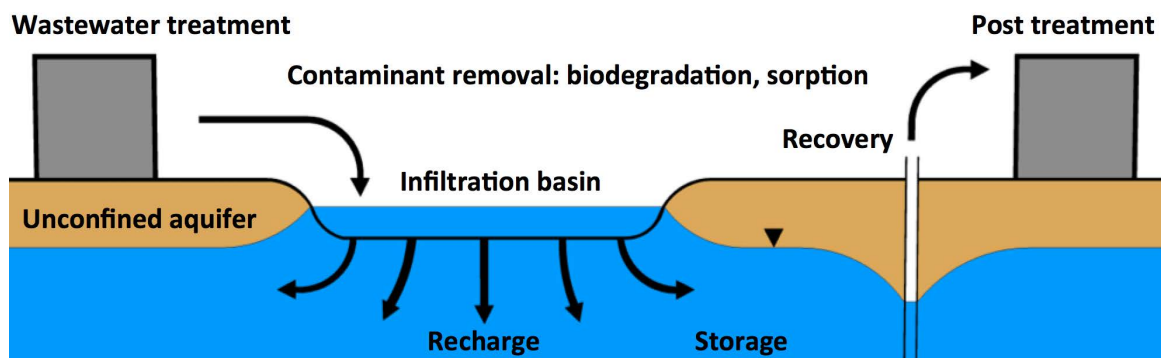


Figure 1.10: Sketch of an aquifer recharge and recovery system for the treatment and storage of post-treatment wastewater.

Although aquifer recharge and recovery systems achieve substantial removal of many trace organic chemicals with biodegradation processes under aerobic conditions (Yoon *et al.*, 2013), system effectiveness and recovery well pumping rates are limited by poor infiltration rates during wet-cycle operation. The hydraulic loading rates of infiltration ponds is observed to decrease over time due to the development of a clogging layer associated with the accumulation of both organic and inorganic fines within near-surface sediments (Ma & Spalding, 1997). Although tilling the surface of infiltration ponds during dry-cycles is utilized in attempts of removing accumulated organic matter and increasing effective near-surface permeability, recharge capacities may remain less than desirable (Bouwer & Rice, 1989). Depending on the amount of fines suspended in the feed water, it can be advantageous to utilize a settling basin (with a non-tilled bottom) to allow for partial settling of the silt load before application to recharge basins (Ma & Spalding, 1997). The increased height of ponded water within infiltration ponds encourages algae growth and organic fines accumulation within near-surface sediments thereby developing the clogging layer and decreasing near-surface permeability (Bouwer & Rice, 1989).

The hydraulic capacity of infiltration ponds is usually expressed as hydraulic loading rate, which is the accumulated infiltration over a long period, including time for dry-cycle infiltration recovery and surface tilling (Bouwer & Rice, 1989). The hydraulic loading rate of infiltration ponds has been observed to vary from about 30 to 300 meters per year and to mostly depend on effective permeability of near-surface sediments (Bouwer & Rice, 1989). The hydraulic loading rate of infiltration ponds is maximized with proper combinations of wet and dry-cycles for surface cleaning and tilling to

mitigate clogging, which is caused by the accumulation of both organic and inorganic fines within near-surface sediments (Bouwer & Rice, 1989). The permeability of the clogging layer can become so low that it becomes the primary control on the hydraulic loading rate of an infiltration pond over time (Bouwer & Rice, 1989). Algae growth within infiltration ponds has the ability to raise the pH of surface water to a range of 8–10, where calcium carbonate can precipitate, accumulate on the bottom, and increase clogging (Bouwer & Rice, 1989).

A comparison of two infiltration ponds constructed within soils of similar permeability indicated that reduced hydraulic loading rate is dominated by increased algae growth and accumulation. Algae growth increases with detention time and lower turnover rates (about once every 10 days in 1 meter of ponded water) (Bouwer & Rice, 1989). The long term hydraulic loading rate in the algae impacted pond was increased by a factor of 5 simply by reducing the ponded water height from 1 to 0.2 meters during wet-cycle operation, which increases turnover rates and reduces algae growth (Bouwer & Rice, 1989). It has also been demonstrated at the laboratory scale that the development of the clogging layer and lower near-surface permeability reduces turnover rates and encourages algae growth (Bouwer & Rice, 1989).

Decreased infiltration rates due to the development of the clogging layer affects redox conditions and retention time in the subsurface, which are key drivers of contaminant removal (Hübner *et al.*, 2012). Aquifer recharge and recovery systems effectively attenuate dissolved organic carbon and effluent-derived organic matter during soil passage under both oxic and anoxic conditions (Yoon *et al.*, 2013). Aquifer recharge and recovery systems are also efficient at removing nitrate and atrazine from effluent-

contaminated water (Ma & Spalding, 1997). A recent study showed that dissolved organic carbon removal was observed to be most efficient under aerobic conditions during the first 2 to 3 days of hydraulic residence time in an aquifer recharge and recovery system (Hübner *et al.*, 2012). Studies have demonstrated that effluent-derived organic matter is comprised of larger molecules and higher amounts of hydrophilic organics, which are preferentially biodegraded over naturally occurring organic matter during aquifer recharge and recovery operation (Drewes *et al.*, 2006).

Advanced oxidation processes within sediment filtration systems have been demonstrated as powerful methods for artificially maintaining oxic conditions, which increases the removal of dissolved organic carbon and many relevant trace organic compounds (Hübner *et al.*, 2012). Artificial ozonation techniques have proven to convert less biodegradable dissolved organic carbon components such as humic and fulvic substances into more biodegradable carbon structures for aquifer recharge and recovery treatment (Yoon *et al.*, 2013). Oxic conditions during subsurface passage are beneficial for many aerobic biological processes (Hübner *et al.*, 2012) and studies have shown that artificially increasing oxidation improves the biodegradability of poorly degradable organic matter in aquifer recharge and recovery systems (Yoon *et al.*, 2013). Bench-scale aerobic aquifer recharge and recovery tests have also verified increased efficiency and removal of bulk organic matter under oxic conditions (Yoon *et al.*, 2013). Near-surface anaerobic conditions are therefore less favorable for wet-cycle aquifer recharge and recovery system operation as most of the organic contaminants of interest biodegrade aerobically (Yoon *et al.*, 2013). Extended wet-cycle aquifer recharge and recovery operation periods could potentially be risky because saturated, near-surface, organic rich,

fine textured floodplain deposits with low specific discharge rates have been observed to develop anoxic conditions followed by anaerobic, microbially mediated, reductive dissolution of authigenic metal-oxides (Smedley & Kinniburgh, 2002).

1.2 Site description

The Aurora Water aquifer recharge and recovery site in Fort Lupton, Colorado, U.S.A, (Figure 1.20) was originally designed by CH2M HILL based on well logs to recharge and recover a predicted 16 million gallons per day (MGD), but is currently capable of about 4 MGD at maximum capacity during wet-cycle operation potentially due to the abundance of authigenic low permeability clay mottled floodplain deposits and the development of the near-surface clogging layers within infiltration ponds.

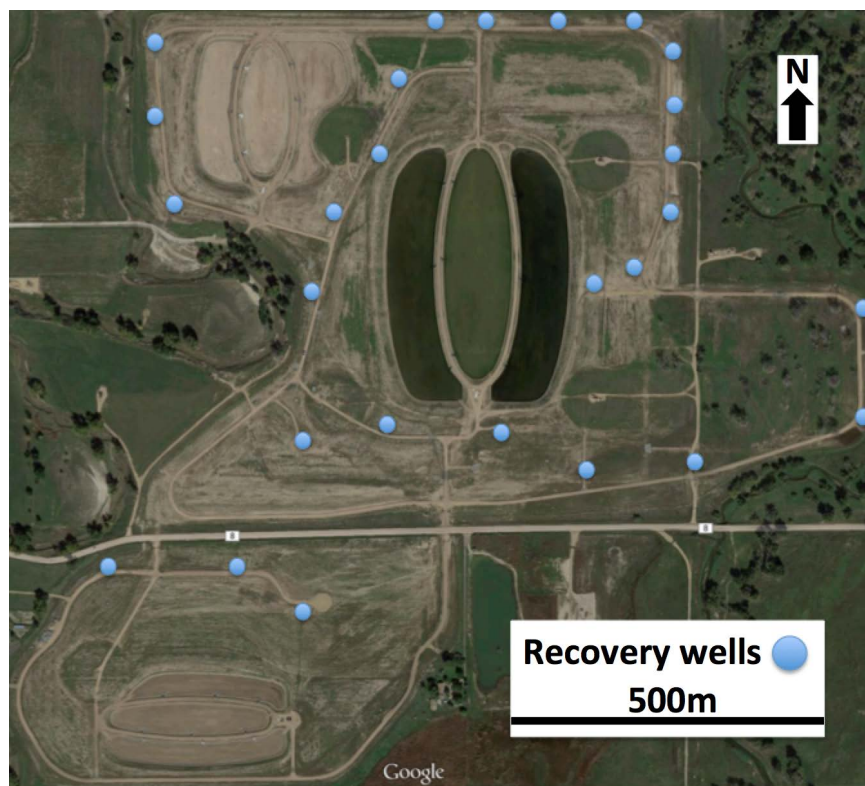


Figure 1.20: The Aurora Water aquifer recharge and recovery site, Fort Lupton, CO.

The highest, most efficient, recovery well pumping rates at the Aurora Water aquifer recharge and recovery site are achieved by several recovery wells to the north, northeast, and east of the eastern central basin (Figure 1.20) with pumping rates up to 400 gallons per minute (GPM). The recovery well just to the south of the eastern central basin can only pump at a maximum rate up to about 230 GPM, which is why it is usually shut off as it less energy-efficient to operate. Previous electrical resistivity surveys at the Aurora Water aquifer recharge and recovery site guided the construction of a new recovery well located to the east of the eastern central basin within more permeable gravely deposits. Gravelly fill deposits at the aquifer recharge and recovery site provide the dominant pathways for pond drainage, groundwater recharge, and recovery. Low permeability shale bedrock underlies the site at about 20 meters depth, which still allows for significant groundwater storage within the overlying sequences of floodplain deposits. A low permeability slurry wall was constructed around the site, which mostly prevents groundwater from flowing offsite. Riverbank aquifers along the South Platte River are pumped downstream of the Aurora Water wastewater treatment facility to supply the infiltration ponds with slightly salty ($\approx 1000 \pm 100 \mu\text{S}/\text{cm}$ based on several surface water samples), nutrient-rich, effluent-contaminated water.

The infiltration ponds at the Aurora Water aquifer recharge and recovery site foster very rapid algae growth during wet-cycle operation and massive algae die-offs due to cold climate conditions (Figure 1.21).



Figure 1.21: Northern view of the algae impacted eastern central infiltration pond, left (10/17/12) is the early stage of a pond flooding and algae growth, center (11/2/12) is the algae impacted stage, and right (11/22/12) shows that the algae has died and settled out.

Rapid algae blooms at the Aurora aquifer recharge and recovery site result from the nutrient-rich floodwater, which could potentially encourage dissolved oxygen depletion at night. Algae growth is observed to be more rapid in the southern area of the eastern central infiltration pond, where surface water could be more stable due to lower near-surface infiltration rates. This is consistent with geophysical observations of very low near-surface discharge rates in the southern area of the eastern central infiltration pond. Massive algae die-offs due to cold climatic conditions occur can occur at the Aurora Water aquifer recharge and recovery site (Figure 1.21). Algae die-offs accumulate organic matter at the ground surface and may encourage dissolved oxygen depletion during wet-cycle operation, where aerobic bacteria may consume remaining dissolved oxygen in the process of decaying the dead algae. Time-lapse redox and dissolved oxygen surveys within surface water and near-surface sediments could be advantageous to provide quantitative information required for better characterizing geochemical and biodegradation processes.

Organic matter accumulates on the ground surface mostly as a result of these massive algae die-offs, which can be transported in the form of dissolved organic matter into the clogging layer ($\approx 20\text{--}30$ cm thick basin-wide based on sediment sampling pits) and lower sediments during wet-cycle operation. The influx of dissolved organic matter is

assumed to encourage microbial growth within the tilled zone during wet-cycle operation. The eastern central pond also becomes thick with bugs and amphibians during wet-cycle operation (Figure 1.23).



Figure 1.23: Amphibians observed during wet-cycle operation at the eastern central pond.

Amphibian biota as well as avian fauna may increase the uptake of nutrients and net bioaccumulation of contaminants within the Aurora Water aquifer recharge and recovery system.

CHAPTER 2 METHODS

2.1 Underwater self-potential

Self-potential methods are utilized to map passive measurements of direct spontaneous current (in mV) at the ground surface with a voltmeter connected to a reference and a roving non-polarizing electrode (Ikard *et al.*, 2012). Self-potential mapping has been utilized for decades for qualitatively locating primary fluid flow pathways through embankments and earthen dams (Jardani *et al.*, 2009). Self-potential signals at the ground surface are influenced by electrical current generated naturally in the subsurface by streaming current associated with advection of excess charge of the diffuse layer (Jardani *et al.*, 2009).

Groundwater flow generates streaming current, where the advective flow of a fraction of the charge contained in the electrical diffuse layer around negatively charged surfaces generates self-potential anomalies (Jardani *et al.*, 2009). Negative self-potential anomalies with respect to a reference arise from streaming current contributions associated with infiltration, higher permeability, and lower electrical conductivity, while relatively positive self-potential anomalies are associated with less infiltration, lower permeability, and increased electrical conductivity (Jardani *et al.*, 2007). The advected charge density (\hat{Q}_V) of the porewater per unit pore volume (in C m^{-3}) can be estimated based on saturated permeability (Figure 2.10).

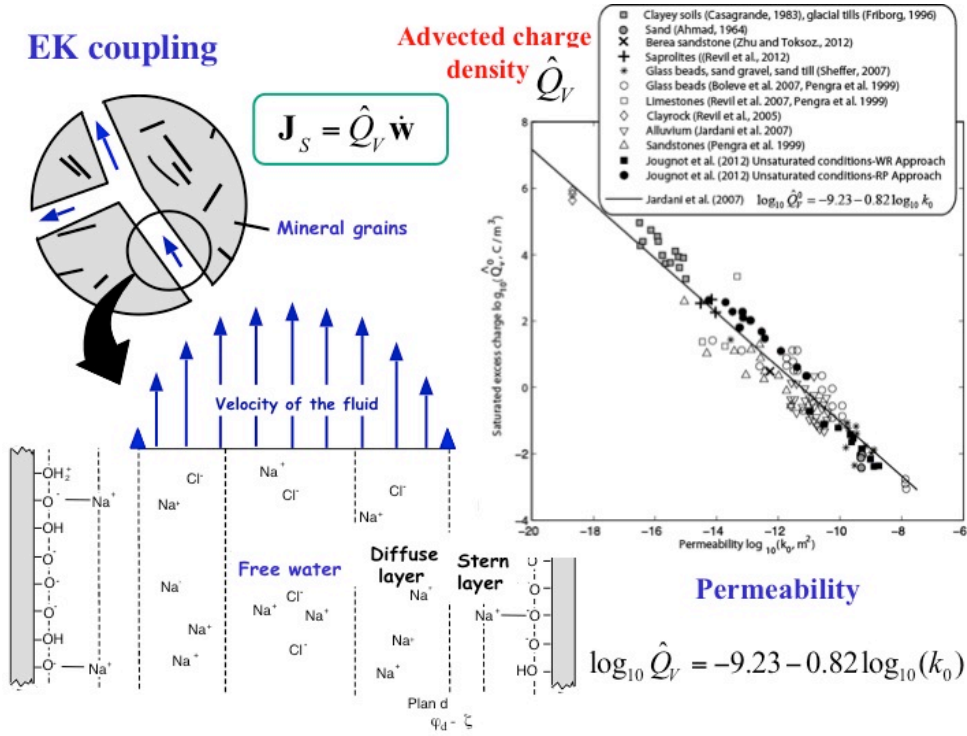


Figure 2.10: Relationship between permeability and advected charge density (Jardani *et al.*, 2007).

The self-potential method has been used to provide information about the permeability and dispersivity of homogeneous media in a controlled sandbox study (Revil *et al.*, 2010). This study demonstrated that the migration of a solute plume creates self-potential anomalies associated with streaming current (Jardani *et al.*, 2009). The streaming current phenomenon requires description with Darcy's law [1] for the Darcy velocity \mathbf{u} (in $m s^{-1}$), Ficks law [2] for the flux of solutes \mathbf{j}_d (in $kg m^{-2} s^{-1}$), and Ohm's law [3] for the current density \mathbf{j} (in $A m^{-2}$):

$$\mathbf{u} = \phi \mathbf{v} = - \left(\frac{1}{\eta_f} \right) \mathbf{k} \cdot (\nabla p + \rho_f g \nabla z), \quad [1]$$

$$\mathbf{j}_d = -\rho_f \phi \mathbf{D} \cdot \nabla C_m + \rho_f \phi \mathbf{v} C_m, \quad [2]$$

$$\mathbf{j} = -\sigma \cdot \nabla \varphi + \hat{Q}_V \mathbf{u}, \quad [3]$$

where \mathbf{v} is the average velocity of porewater (in m s^{-1}), \mathbf{k} is the permeability tensor (in m^2), \mathbf{D} is the hydrodynamic dispersion tensor (in m^2s^{-1}), σ is the electrical conductivity tensor (in S m^{-1}) of the porous material, ϕ is the unitless connected porosity, p is the pore pressure (in Pa), φ is the self-potential (in V), C_m is the unitless solute mass fraction, η_f is the dynamic viscosity of the fluid (in Pa s), ρ_f is the solute bulk density (in kg m^{-3}), g is gravity = 9.81 m s^{-2} , and \hat{Q}_V is the advected charge density of the porewater per unit pore volume (in C m^{-3}) (Jardani *et al.*, 2009). The source current density contribution from the streaming current density is defined as \mathbf{j}_S (in A m^{-2}), which is equal to $\hat{Q}_V \mathbf{u}$ in equation [3] (Ahmed *et al.*, 2013). The charge density \hat{Q}_V can be predicted with the following equation:

$$\log(\hat{Q}_V) = -9.2 - 0.82 \log(k), \quad [4]$$

where k is intrinsic permeability (in m^2) (Jardani *et al.*, 2007). For partially saturated media, the electrical current density (\mathbf{j}) of a medium is dependent on volumetric water content (θ), which is expressed with previously defined units in the following equation:

$$\mathbf{j} = -\sigma(\theta)\nabla\varphi + \hat{Q}_V \left(\frac{\phi}{\theta}\right) \mathbf{u}, \quad [5]$$

where Darcy velocity tensor (\mathbf{u}) is solved with Richard's equation, which accounts for relative hydraulic conductivity within less than fully saturated media (Revil *et al.*, 2010).

For saturated media, excess charge density \hat{Q}_V depends mostly on intrinsic permeability and groundwater velocity (Revil *et al.*, 2010). The continuity for the electrical charge is given by the following equation:

$$\nabla \cdot \mathbf{j} = 0, \quad [6]$$

where the divergence of current density (\mathbf{j}) is zero (Revil *et al.*, 2010). Forward modeling self-potential responses to groundwater flow requires computing ground water velocity to resolve for source current density, which allows the solution of a Poisson equation for self-potential estimations (Ahmed *et al.*, 2013). The relative self-potential response to infiltration is well demonstrated with numerical simulations in COMSOL Multiphysics (Jardani *et al.*, 2007) (Figure 2.11).

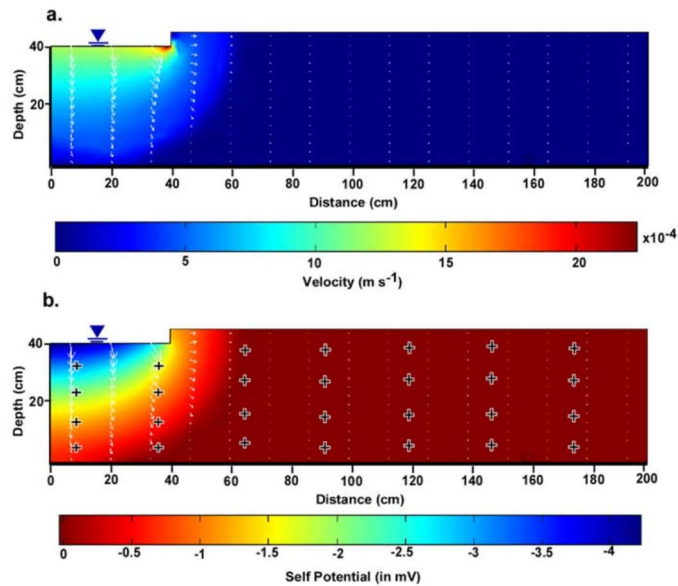


Figure 2.11: Numerical COMSOL simulation of the relative negative self-potential response (a) to groundwater infiltration (b) (Jardani *et al.*, 2007).

Negative underwater self-potential anomalies are theoretically dominated by increased permeability and streaming current contributions associated with infiltration, coarser sediment textures, and higher porewater velocities with lower near-surface excess charge densities in diffuse layers around negatively charged surfaces (Figure 2.12).

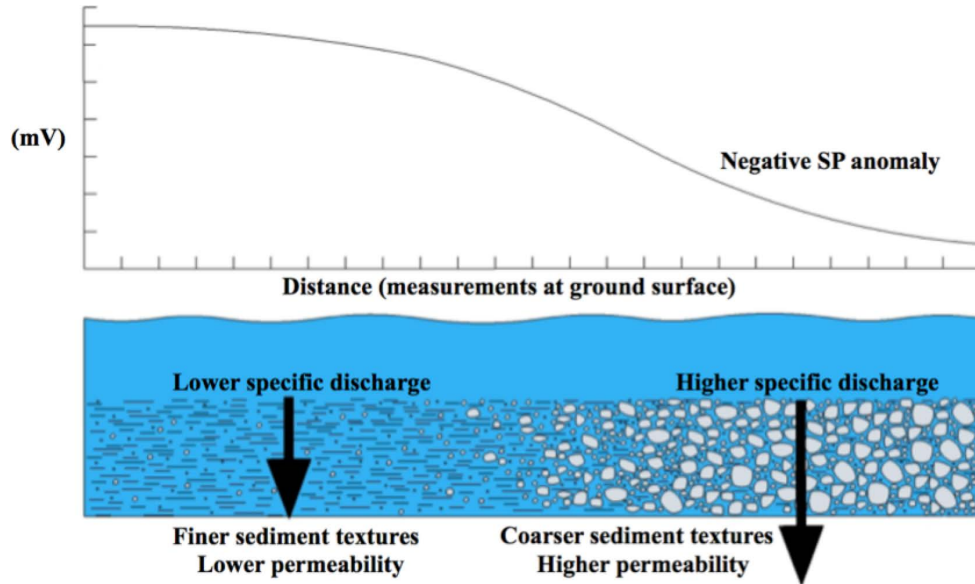


Figure 2.12: Sketch of self-potential anomaly. Relatively negative underwater self-potential signals at the ground surface are associated with coarser sediment textures, increased porewater velocities, and lower excess charge densities. Relatively positive self-potential signals are induced by lower permeability, higher excess charge densities, lower specific discharge, and finer sediment textures.

Finer near-surface sediment textures that restrict porewater flow result in lower streaming current contributions and increased excess charge densities within porewater (Revil *et al.*, 2010). It has been demonstrated that self-potential data can be inverted to groundwater flow velocity with inverse modeling in COMSOL, and that permeability is a dominating source for self-potential anomalies (Revil *et al.*, 2010).

Negative self-potential anomalies associated with infiltration above the water table are proportional to the thickness of the vadose zone (Jardani *et al.*, 2007), which is proposed by the following equation:

$$H(x, y) = h(x, y) - e_0 - \varphi(x, y)/c, \quad [7]$$

where $H(x, y)$ is the elevation of the water table with respect to a datum, $h(x, y)$ is elevation of the ground surface self-potential measurement station, e_0 is the thickness of the vadose zone, $\varphi(x, y)$ is the measured self-potential signal, and c is the apparent

voltage coupling coefficient (in mV/m) (Jardani *et al.*, 2007). We assume that ground surface self-potential surveys have increased noise mainly due to variably saturated conditions and contributions to self-potential signals from equations [5] and [7].

Underwater self-potential measurements within wetted media are therefore advantageous for detecting streaming current contributions to self-potential signals because it removes the saturation variables from equations [5] and [7].

Electrical resistivity tomography has been used as complementary information when combined with self-potential and electromagnetics surveys because it provides spatial information about saturation, salinity, and sediment textures at depth, with strong vertical resolution (Jardani *et al.*, 2007). Temperature changes that induce drift in self-potential measurements are assumed to have negligible contributions because a 10°C change is responsible for only 2 mV measurement drift (Ikard *et al.*, 2012). The underwater scanning electrode drift can be negligible ($\approx +4$ mV) over underwater self-potential survey periods and is easily corrected for with the non-polarizing reference electrode.

2.2 High-resolution temperature sensing

High-resolution temperature sensing methods utilize temperature as a naturally occurring groundwater water tracer to estimate specific discharge (Briggs *et al.*, 2012). The movement of groundwater through saturated and unsaturated zones between aquifers and surface-water bodies can be estimated with temperature measurements (Anderson, 2005). Temperature measurements used to be limited to reach-average parameters or discrete point measurements, but now emerging technologies allow for the collection of

temperature measurements at high spatial and temporal resolution over long sensor lengths (Tyler *et al.*, 2009). Distributed temperature sensing units provide estimated temperature measurements across long distances of fiber-optic cable (up to 30,000m) with high (up to 0.01 °C) sensitivity (Selker *et al.*, 2006). Distributed temperature sensing units can be utilized to determine the spatial variability of groundwater discharge by measuring temperature variations along streambeds with high temporal resolution over long distances (Tyler *et al.*, 2009). Distributed temperature sensing units are also utilized to quantify surface water-groundwater exchange in rivers and streams with high spatial resolution temperature measurements (Selker *et al.*, 2006).

Temperature estimates with distributed temperature sensing units are usually resolved to one meter resolution because spectra can only be accurately measured every 20 ns after an injection of light, which is the time it takes light to travel 2 meters by propagating and reflecting back along 1m of glass fiber (Selker *et al.*, 2006). One-meter spatial resolution measurements are useful for reach-scale streambed studies to determine spatial variability of surface water-groundwater exchange (Tyler *et al.*, 2009). Vertical high-resolution temperature data are increasingly used to estimate hyporheic flow in response to recent increased interest in the hyporheic zone (Voytek *et al.*, 2013). High-resolution temperature sensing methods are conducted by coiling fiber-optic cable to provide much higher spatial resolution to temperature measurements, which can then be used for estimating groundwater advection in saturated media from ambient diurnal temperature patterns within streambeds (Briggs *et al.*, 2012).

Studies have successfully implemented high-resolution temperature sensing within streambeds to estimate seepage from measured high-resolution diurnal

temperature patterns associated with heat conduction and groundwater advection (Constantz, 2008). Analysis of long time series high-resolution temperature-sensing data can be conducted with dynamic harmonic regression to obtain the diurnal temperature signal, where the phase angles and amplitudes of temperature fluctuations are utilized to calculate temperature attenuation at depth over time, which can be converted to seepage rate (Vogt *et al.*, 2010). Quantitative description of the spatial and temporal variability of vertical hyporheic flux into streambeds induced by dam structures has also been successfully studied with the high-resolution temperature-sensing method (Briggs *et al.*, 2012).

High-resolution 1D vertical temperature profiles can be analyzed by calibrating numerical models to match observed data with a variety of time-varying temperature boundary conditions, varying head conditions, and heterogeneity of sediments with depth (Voytek *et al.*, 2013). Properties such as sediment heat capacity and sediment thermal conductivity effect heat attenuation at depth within groundwater systems (Healy, 1990), where diurnal temperature changes within streambeds can be either conduction dominated or advection dominated (Briggs *et al.*, 2012). The space domain of temperature measurements along a fiber-optic cable is limited by the intensity of laser and the sensor performance, or the ability of the distributed temperature sensing unit to resolve a backscatter signal, which degrades due to the dispersion of light and decay over a length of glass fiber (Tyler *et al.*, 2009).

Distributed temperature sensing units function by measuring backscatter signals along a glass fiber after light injections, where the ratio of amplitude differences within the Raman spectra backscatter signals (Stokes and anti-Stokes) depends on the density

and temperature of the glass fiber (Selker *et al.*, 2006). Return signal strength also depends on the diameter of the glass fiber, where larger diameter (50 μ m) fibers have return signal strength about 25 times greater than standard (9 μ m) fibers (Selker *et al.*, 2006). Distributed temperature sensing units can adsorb and filter particular frequencies within the Raman spectra (Selker *et al.*, 2006) (Figure 2.20).

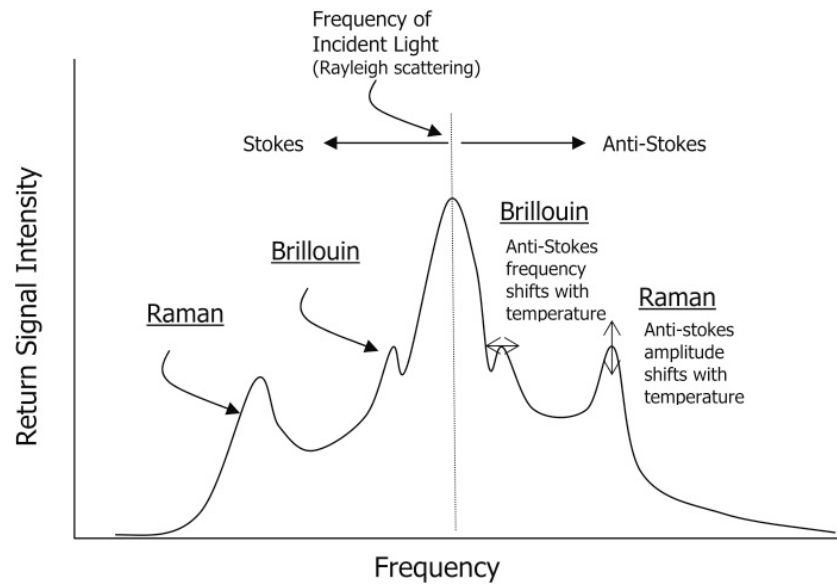


Figure 2.20: Diagram of the return signal intensity below and above the frequency of injected light (Selker *et al.*, 2006).

The backscattered Stokes signal is produced when photons increase the vibrational state of silica molecules, while backscattered anti-Stokes signal is produced when the vibrational state of previously excited silica molecules is decreased during collisions with incident photons (Figure 2.20) (Selker *et al.*, 2006). Therefore, as the temperature of the glass fiber increases, the frequency of photon collisions with previously excited silica molecules increases (Tyler *et al.*, 2009). Elastic (Rayleigh) scattering does not change wavelength within the return signal, while nonelastic scattering phenomena induces the Brillouin, Stokes, and anti-Stokes light wavelengths (Tyler *et al.*, 2009). The wavelength

shift of the injected light into Stokes and anti-Stokes is proportional to acoustic velocity within the fiber, which is a function of fiber density and temperature (Selker *et al.*, 2006). The magnitude of the Raman Stokes scattering is a linear function of light intensity while the anti-Stokes scattering is both a linear function of light intensity and an exponential function of fiber temperature (Selker *et al.*, 2006). The ratio of the magnitudes of the anti-Stokes to Stokes signals eliminates the light intensity dependence on temperature estimations (Tyler *et al.*, 2009). Temperature time-series measured by distributed temperature sensing units are easily corrected with temperature datums (ice baths) to correct error due to linear backscatter decay along the fiber-optic cable (Selker *et al.*, 2006).

Analysis of one-dimensional high-resolution temperature profiles under saturated conditions can be conducted with 1DTempPro, which runs the VS2DH code to solve flow and energy transport equations (Voytek *et al.*, 2013). 1DTempPro is a program that allows users to calibrate 1D VS2DH models with temperature time-series data in order to efficiently discretize estimations of flux at different depths (Voytek *et al.*, 2013). The calibration workflow for 1D VS2DH models in 1DTempPro is shown below (Figure 2.21).

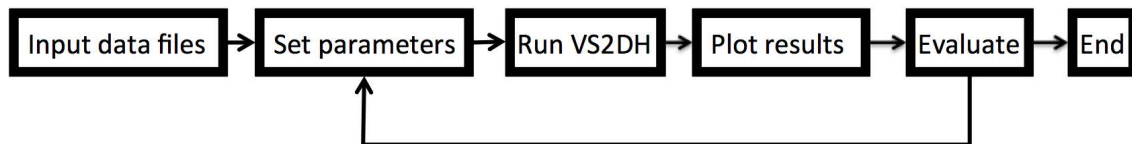


Figure 2.21: Calibration workflow in 1DTempPro for running the VS2DH code and estimating specific discharge.

1DTempPro assumes homogeneous saturated sediments with active cells surrounded by no-flow boundaries (Healy, 1990). The finite difference approach is applied to solve the advection-dispersion equation for single-phase liquid water, which is

used to describe energy transport (Healy, 1990). Changes in energy stored within saturated porous media occur due to water of different temperature flowing into the media, thermal conduction into and out of the media, and energy dispersion into and out of the media (Healy & Ronan, 1996). The energy transport equation [8] for the VS2DH code is a form of the advection-dispersion equation, written with temperature as the dependent variable:

$$\frac{\partial}{\partial t}(\theta C_w + (1 - \phi)C_s)T = \nabla \cdot K_T(\theta)\nabla T + \nabla \cdot \theta C_w D_H \nabla T - \nabla \theta C_w v T + q C_w T^*, \quad [8]$$

where t is time (in s), θ is volumetric water content, C_w is heat capacity of water (in J/m³°C), ϕ is porosity, C_s is heat capacity of the dry solids in (J/m³°C), T is temperature (in °C), K_T is the thermal conductivity of the water and solid matrix (in W/m°C), D_H is hydrodynamic dispersion (in m²/s), v is water velocity (in m/s), q is rate of fluid source (in s⁻¹), and T^* is temperature of fluid source (in °C) (Healy & Ronan, 1996). The VS2DH energy transport equation [8] ignores the heat capacity of the air phase when the medium is less than fully saturated (Healy & Ronan, 1996). Obtaining high-resolution temperature sensing measurements under fully saturated conditions is therefore advantageous, where the air heat capacity is relatively small compared to water and heat conduction is strongly dependent on moisture content (Healy & Ronan, 1996). The left of equation [8] is the change in energy stored in a volume over time while the first term on the right side of equation [8] accounts for energy transport due to conduction within the saturated media (Healy & Ronan, 1996). The dispersive and advective terms on the right side of the energy transport equation [8] are analogous to solute transport advection dispersion equations, while the last term on the right accounts for heat sources and sinks (Healy & Ronan, 1996). The movement of water through the saturated media induces

energy transport due to mixing, which is defined as the thermo-mechanical dispersion tensor (Healy & Ronan, 1996). Mechanisms for heat conduction are analogous to mechanisms of water flow, where thermal conductivity is similar to hydraulic conductivity, and temperature gradient is similar to head gradient (Selker *et al.*, 2006). Groundwater advection transports energy by the movement of water of different temperatures, which is analogous to the advective transport of solutes in groundwater (Selker *et al.*, 2006). The flow equation [9] solved by the VS2DH code accounts for the temperature dependency of groundwater viscosity, where saturated hydraulic conductivity, K , is a function of temperature:

$$K = \rho g k / \mu(T), \quad [9]$$

where ρ is density (in kg/m³), g is gravity (in m/s²), k is intrinsic permeability (in m²), and μ is the temperature dependent viscosity of water (in Ns/m²) (Healy & Ronan, 1996). The temperature dependence on groundwater density is assumed to be negligible (Healy & Ronan, 1996). The flow equation [9] is solved first within each time step assuming a temperature equal to the previous time step (Healy & Ronan, 1996). The energy transport equation [8] is solved next to update the value of temperature (Healy & Ronan, 1996). The flow equation [9] is then resolved with the updated temperature (Healy & Ronan, 1996). This iterative process is continued within each time step up to 4 or 5 times until velocity changes between solutions of the flow equation [9] are less in magnitude than the velocity closure criterion in the energy transport equation [8] at every node (Healy & Ronan, 1996). Studies have utilized sliding windows of analysis across high-resolution temperature-sensing probe data to better discretize groundwater flux at different depths (Briggs *et al.*, 2012), but for the sake of simplicity, this study will utilize

1DTempPro to break up high-resolution temperature-sensing data into discrete 14cm layers with 0.02 m vertical resolution to estimate specific discharge from temperature measurements.

2.3 Electrical resistivity tomography

Electrical resistivity tomography provides spatial information of resistive material properties by injecting current and measuring electrical potential (Revil *et al.*, 2012).

Electrical resistivity tomography is sensitive to the mineralogy, saturation, temperature, and the electrical conductivity of sediments and porewater (Revil *et al.*, 2012). The electrical conductivity of a porous medium σ_0 (in S m⁻¹) is the reciprocal of the electrical resistivity ρ_0 (in ohm-m) (Revil *et al.*, 2012). An electrical current within a porous medium represents the flux of charge carriers, which can be ions or electrons. The fundamental constitutive equation governing the flux of charge carriers is Ohm's law, which relates current density \mathbf{j} (in A m⁻²) to the electrical field \mathbf{E} (in V m⁻¹):

$$\mathbf{j} = \sigma_0 \mathbf{E}, \quad [10]$$

$$\mathbf{E} = -\nabla\varphi, \quad [11]$$

where φ is the electrical potential (in V) (Revil *et al.*, 2012). As an injected current enters a volume, it destroys the self-potential field and then leaves the volume, so we assume continuity where there is no storage of electrical charges inside porous material, which leads to the Poisson equation:

$$\nabla \cdot (\sigma_0 \nabla \varphi) = 0, \quad [12]$$

which simplifies to the Laplace equation within homogeneous media (Revil *et al.*, 2012).

In order to measure resistivity, two electrodes (A and B) are used to inject and retrieve

current while at least two other electrodes (M and N) are used to measure the drop in the electrical potential associated with the injected current, which is described by Ohm's law with the following equation:

$$U = \varphi(M) - \varphi(N) = I\rho/g, \quad [13]$$

where U is the voltage difference in electrical potential between electrodes M and N for a homogeneous material with resistivity ρ , I is the strength of the injected current, and g is the geometrical factor (in m) (Revil *et al.*, 2012). The geometrical factor for resistivity measurements within a half-space depends on the position on the electrodes, which is given by the following equation:

$$g = 2\pi/(\frac{1}{AM} - \frac{1}{BM} - \frac{1}{AN} + \frac{1}{BN}), \quad [14]$$

where AM, BM, AN, and BN represent the distances between electrodes (in m) (Revil *et al.*, 2012). Wenner geometry has equal spacing between electrodes for resistivity measurements, which provides the best signal to noise ratio within tabular media, making it advantageous for characterizing relatively horizontally layered floodplain deposits (Revil *et al.*, 2012). The measured resistance multiplied by the geometrical factor yields the apparent resistivity, which represents a weighted average of true resistivity in the medium between the A and B electrodes, where apparent resistivity equals the true resistivity of a homogeneous material (Revil *et al.*, 2012). True resistivity of heterogeneous materials can be obtained through the inversion of apparent resistivity (Revil *et al.*, 2012). Inverse modeling can be utilized to construct tomograms by applying the finite element or finite difference method to solve the Poisson equation (Revil *et al.*, 2012). The inverse resistivity model, or tomogram, better explains the distribution of measured apparent resistivity data by smoothing data and applying boundary conditions

(Revil *et al.*, 2012). Modern electrical resistivity units, such as the ABEM Terrameter used in this study, utilize automatic switching boxes, which allows for a large number of resistivity measurements at many stations over long distances in a short period of time (Revil *et al.*, 2012). Electrical resistivity tomography typically images well-drained sediments (sands and gravels) as more resistive zones, whereas finer grained sediments with more silts and clays, which hold more water by capillarity, are imaged as more conductive zones (Clément *et al.*, 2009).

Time-lapse electrical resistivity tomography is a powerful method, capable of imaging hydrodynamic processes, such as differences in the infiltration of water within fine sediment textures or coarser sediment textures (Oldenborger *et al.*, 2007). Time-lapse electrical resistivity tomography is also sensitive to changes in the total dissolved solids, which is important in environmental applications that seek to image the drainage pathways for groundwater contaminants or the migration of contaminant plumes (Revil *et al.*, 2012). When sediments are partially saturated, the relationship known as Archie's law can be modified to solve for volumetric water content (θ) based on electrical conductivity with the following equation:

$$\theta = \left(\frac{\sigma_t}{a\sigma_w\phi^m} \right)^{1/n}, \quad [15]$$

where σ_t is the modeled electrical conductivity (in S/m), σ_w is the electrical conductivity of the porewater (in S/m), ϕ is porosity, and a , m , and n are fitting parameters (Miller *et al.*, 2008). For infiltration time-lapse electrical resistivity tomography monitoring, the greatest negative changes in resistivity over time at depth are attributed to increased saturation within coarser, more permeable, sediments (Oldenborger *et al.*, 2007).

Inversely, for draining groundwater conditions and time-lapse electrical resistivity

tomography monitoring, the greatest positive changes in resistivity over time are attributed to decreased saturation within coarser, more permeable sediments (Daily *et al.*, 1992).

2.4 Electromagnetics

Electromagnetics methods provide spatial information of measured apparent electrical conductivity of a medium at depth by taking quadrature measurements of the secondary electromagnetic fields generated in the subsurface after the transmission of electromagnetic radiation above the ground surface. Ground conductivity meters, such as the Geonics EM-31 utilized in this study, can measure apparent conductivity of subsurface materials, which is influenced by saturation, solute content, and mineralogy (Morris, 2009). Electromagnetics surveys are utilized for a wide range of applications, including salinity mapping, soil mapping, groundwater mapping, and contaminant plume mapping (Morris, 2009). Apparent conductivity measurements with EM-31 units are weighted averages of the electrical conductivity at depth, where the EM-31 receiver measures the secondary magnetic field response curve (Morris, 2009). The half depth of EM-31 measurements represents the depth where half of the secondary electromagnetic response is assumed to be generated above and the other half of the electromagnetic response is generated below, which is estimated to be at about 3 m depth for an EM-31 unit located less than 1m above the ground surface (Morris, 2009). Heterogeneities in the field affect the measured apparent conductivity, where the thicker a higher conductivity top layer is, the greater its contribution to apparent conductivity readings will be (Morris, 2009). Changing the height of an EM-31 unit less than 1m above the ground surface

during electromagnetics surveys does not significantly lose depth penetration or sensitivity to changes in measured apparent conductivity in the subsurface (Morris, 2009).

2.5 Laboratory electrical resistivity tests

The mineralogical compositions of sediment samples can be characterized with low-frequency lab resistivity tests conducted with a high-accuracy impedance spectrometer system (Zimmermann *et al.*, 2008). Impedance spectrometer systems can measure complex voltage within a range from 1 mHz to 45 kHz and function with two electrodes for current injection and two electrodes for voltage measurements (Zimmermann *et al.*, 2008). Resistivity tests can therefore be conducted with impedance spectrometer systems in a laboratory at low frequencies (1, 10, and 100 Hz), where sediment samples can be saturated with fluids of known electrical conductivity. The geometrical factor of the container used for packing and saturated sediment samples can be determined by measuring the apparent resistivity of several different fluid samples with known electrical conductivities.

CHAPTER 3 RESULTS

3.1 Underwater self-potential

The underwater self-potential method was developed to measure self-potential signals at the ground surface with ± 10 meter gridding throughout a flooded infiltration pond during recovery well pumping. The reference electrode is used to correct for electrode drift during the measurement period, which can be negligible ($\approx +4$ mV) over ≈ 6 hour survey periods when the reference electrode is located in a stable environment above the water table, buried at least one foot deep within compacted clay in the western berm and shaded from the sun. The initial seven underwater self-potential surveys were incomplete and had problems with too low of ponded water heights, cord breakage, voltmeter breakage, electrode breakage, roving electrode drift, and the accumulation of hundreds of pounds of algae on the traveling cord. Time-efficiently removing the huge algae masses that accumulate on the traveling cord with each pass across the infiltration requires a large knife, which increases the risk of cord breakage. Cord breakage occurs when the rubber cladding is sliced or kinked to the point where the metal core is exposed.

The electrical conductivity distribution in surface water is observed to have negligible differences ($\approx \pm 5$ $\mu\text{S}/\text{cm}$) across the eastern central pond by collecting large surface water samples from the far north and far south and measuring water conductivity shortly after in a lab. The successful underwater self-potential surveys started with non-polarizing electrodes, which produced self-potential signals of 0 mV when wetted and pressed face to face and had low electrode drift (with $\approx +4$ mV reference correction at the

end of each survey). The two successful underwater self-potential surveys #1 and #2 were conducted during constant recovery well pumping, two feet of standing water, and flooding input within the eastern central pond (Figure 3.10).

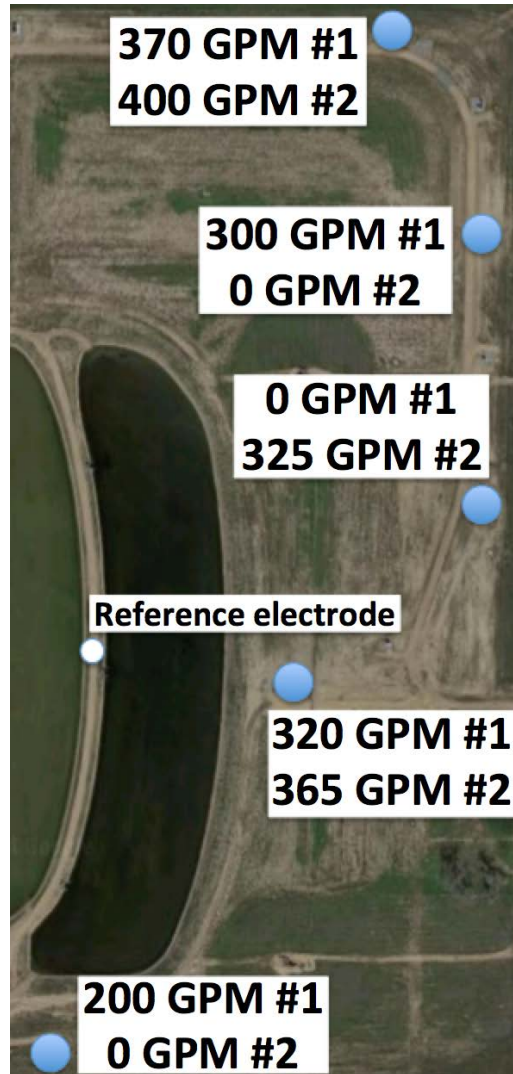


Figure 3.10: Recovery well pumping rates (in GPM) at active recovery wells during underwater self-potential surveys #1 (9/28/13) and #2 (10/8/13) with the reference electrode location in the western berm.

Each underwater self-potential measurement requires gently pressing the scanning electrode into surface sediments underwater with a staff and up to 10 to 15 seconds of waiting time for the scanning electrode to equilibrate with the dominating porewater self-potential signal by watching value (in mV) on the voltmeter level out and remain

constant. The underwater self-potential surveys were plotted using SURFER11 for spherical Kriging between measurement points, which were recorded with a GPS in UTM coordinates (Figure 3.11).

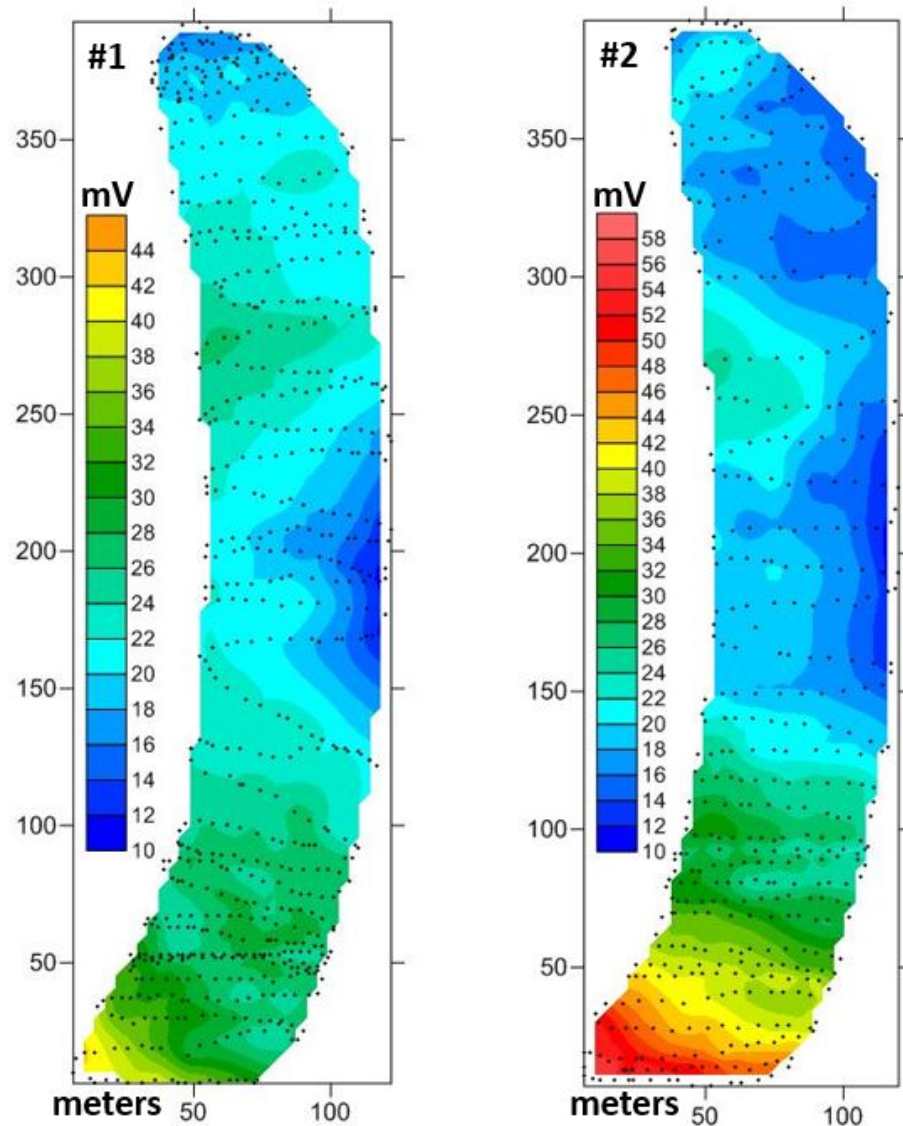


Figure 3.11: Plot of underwater self-potential surveys #1 (9/28/13) and #2 (10/8/13) (dots are measurement points). Surface water conductivity for underwater self-potential survey #1 was 1007 $\mu\text{S}/\text{cm}$ in the far north and 1012 $\mu\text{S}/\text{cm}$ in the far south. Surface water conductivity for underwater self-potential survey #2 was 986 $\mu\text{S}/\text{cm}$ in the far north and 992 $\mu\text{S}/\text{cm}$ in the far south.

Negative contributions to underwater self-potential signals in the infiltration pond (Figure 3.11) appear to be associated with the recovery well pumping regimes (Figure 3.10),

where greater pumping rates could induce higher porewater velocities near the ground surface within coarser, more permeable, sediments proximal to well locations. Recovery wells to the northeast and east of the pond with increased pumping between surveys #1 and #2 (Figure 3.10) could have contributed to the lower underwater self-potential signals in survey #2 (Figure 3.11) due to increased infiltration and streaming current contributions. The recovery well to the south of the basin was turned off after underwater self-potential survey #1 (Figure 3.10), which may explain why survey #2 has significantly more positive underwater self-potential values in the south of the basin (Figure 3.11) associated with less infiltration, lower streaming current contributions, finer sediment textures, lower permeability, and greater excess of charges within diffuse layers around negatively charged surfaces. Electrical conductivity differences in northern and southern surface waters ($\approx \pm 5$ uS/cm) observed during underwater self-potential surveys #1 and #2 is assumed to have a negligible contribution to the observed differences in self-potential signals, which are theoretically dominated by differences in streaming current, permeability, and near-surface groundwater velocity.

3.2 High-resolution temperature sensing

A method for high-resolution temperature sensing was developed to monitor groundwater flow by using heat as a groundwater tracer in the eastern central infiltration pond at the Aurora Water aquifer recharge and recovery site. An array of high-resolution temperature sensing probes was constructed with 2 meter long epoxy fiberglass rods to have a more-similar thermal conductivity to the surrounding sediments than metal rods. The large rod diameter of 2 inches is required to avoid the critical bend angle of fiber-

optic cable that restricts internal reflections and the flow of photons. Termination of the light injections was achieved by wrapping the fiber-optic cable around a pencil at the end of the single-ended high-resolution temperature sensing probe array. Epoxy fiberglass rods were threaded with an acme-form die on a lathe by hand because the lathe at Colorado School of Mines did not have enough torque to machine the threading with the die (Figure 3.20).



Figure 3.20: Threading epoxy fiberglass rods by hand requires the use of a lathe to hold the epoxy fiberglass rod in place while one to two people use lever arms to turn the die quarter turns at a time with brute force, which can boil lubricant and burn epoxy fiberglass.

Attempts of machining the threading form on a larger industrial lathe at Warren Tech, CO, proved unsuccessful due to the overheating and burning of epoxy at the lowest possible turning rate. The array was intended to consist of 20 high-resolution temperature sensing probes based on the 5 km fiber-optic cable capacity of the SEN2-SR distributed temperature sensing unit utilized in this study. Time constraints due to the aquifer recharge and recovery site operation plan and slow construction provided 4 high-resolution temperature sensing probes. The 50 μm diameter glass fiber was coated with

acrylic and protected with 1.17 mm diameter steel cladding, which was then inlaid into the acme-treading form so that the high-resolution temperature sensing probes had a vertical resolution of 2 cm (Figure 3.21).

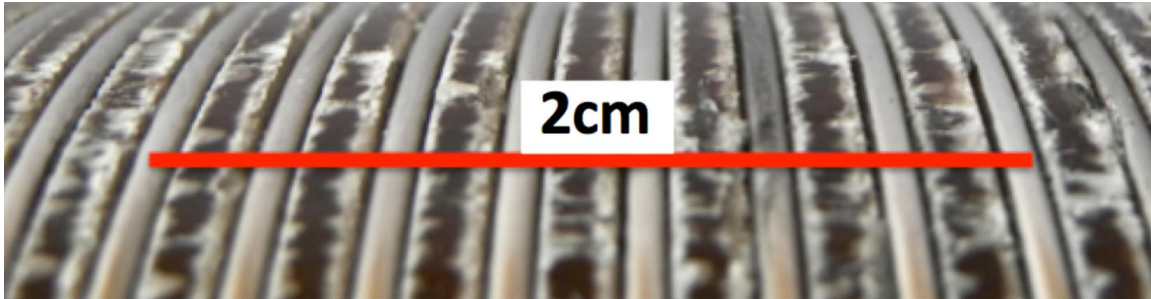


Figure 3.21: 1 m of fiber-optic cable coiled along the 2 inch diameter rods results in 2 cm vertical resolution, where the 1.17 mm diameter steel clad fiber-optic cable lays about 0.1 mm below the outer epoxy fiberglass surface to provide both cable protection during insertion and good contact with the sediments and porewater.

The top of the high-resolution temperature sensing probes is constructed to accommodate a large pin for probe removal and reuse. The incoming fiber-optic cable coils down the high-resolution temperature sensing probes from the top while the outgoing fiber-optic cable exits through the inner core and a slit carved into the top (Figure 3.22).

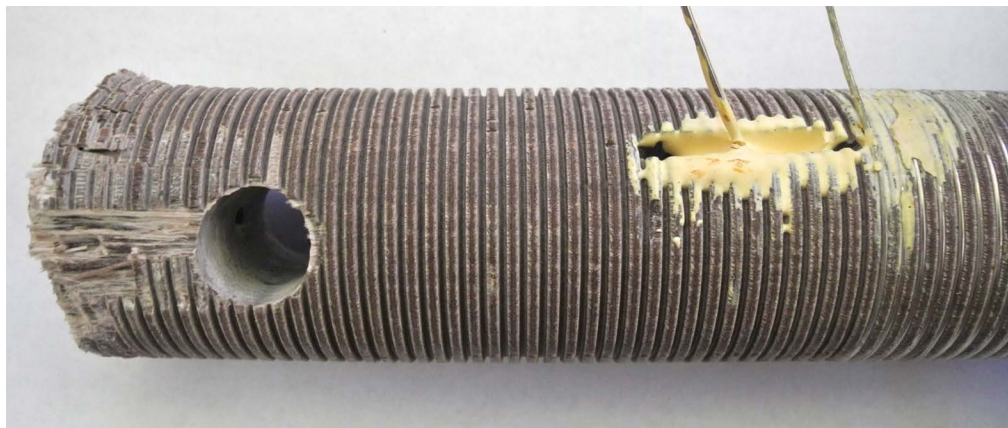


Figure 3.22: The top of a recovered high-resolution temperature sensing probe, where the fiber-optic cable is held in place with epoxy resin. Damage at the top resulted from the probe insertion method with the backhoe.

The bottom of the high-resolution temperature sensing probes required steel drive points (constructed by hand on a lathe), which were sometimes lost during probe removal with

the backhoe. To avoid the critical bend angle of fiber-optic cable, a curving trough is carved into the surface of the epoxy fiberglass rod to align the cable with a wide slit that allows the cable to be fed up through the inner core to the next high-resolution temperature sensing probe (Figure 3.23).



Figure 3.23: The bottom of a recovered high-resolution temperature sensing probe, where the fiber-optic cable does not exceed the critical bend angle and is protected with epoxy resin. The cable exits through the curved trough, slit, and up through the inner rod core. (Not original drive point).

The fiber-optic cable between high-resolution temperature sensing probes was connected with a Fujikura arc-fusion splicer to construct the single ended high-resolution temperature sensing probe array (Figure 3.24).



Figure 3.24: The Fujikura arc-fusion splicer utilizes a microscope to image splices and then references a library of splice images with known optical losses of light (in dB) to estimate the optical loss due to the splice. Splices for the high-resolution temperature sensing probe array were only accepted with estimated 0.0 dB losses.

The high-resolution temperature sensing experiment was single ended, where the fiber-optic cable is terminated by the method of wrapping it around a pencil in the distal ice

bath datum. Two ice baths were used as temperature datums at the beginning and end of the fiber-optic cable, each containing 20 meters of coiled cable and independent HOBO temperature probes located at the center of each cable coil for correcting drift in temperature measurements due to linear backscatter decay, which can vary over time. Constant temperature in the ice baths was well maintained by adding 25 pounds of ice per hour to maintain a homogeneous slushy of ice within each datum. The high-resolution temperature sensing probes were inserted in situ with a backhoe and measurements were taken during fully saturated conditions, recovery well pumping, and pond flooding with relatively colder water (Figure 3.25).

High-resolution temperature sensing



Figure 3.25: In situ high-resolution temperature sensing probe insertion with a backhoe, probe locations, and steady pumping rates during the experiment. Probe 4 was located just east of probe 3, but signal was lost due to cable breakage at some point along probe 4 possibly due to scraping a large cobble during direct push insertion.

The water table at the eastern central pond at the beginning of the high-resolution temperature sensing experiment was ≈ 5 cm below the ground surface basin-wide, so we

assume fully saturated conditions throughout the measurement period and only model data below 6 cm depth. Temperature changes in the high-resolution temperature sensing data associated with cold groundwater advection during the first day of flooding and groundwater pumping were used to for modeling with 1DTempPro, which runs the VS2DH code to numerically solve saturated-flow and heat-transport equations (Voytek *et al.*, 2013). Thermal conductivity and heat capacity tests were conducted in a lab with a Decagon KD2Pro on saturated sediment samples from the tilled zone (5–20 cm) and the lower native sediments (30–45 cm) at the probe locations to improve initial parameterization of the 1DTempPro models (Figure 3.26).

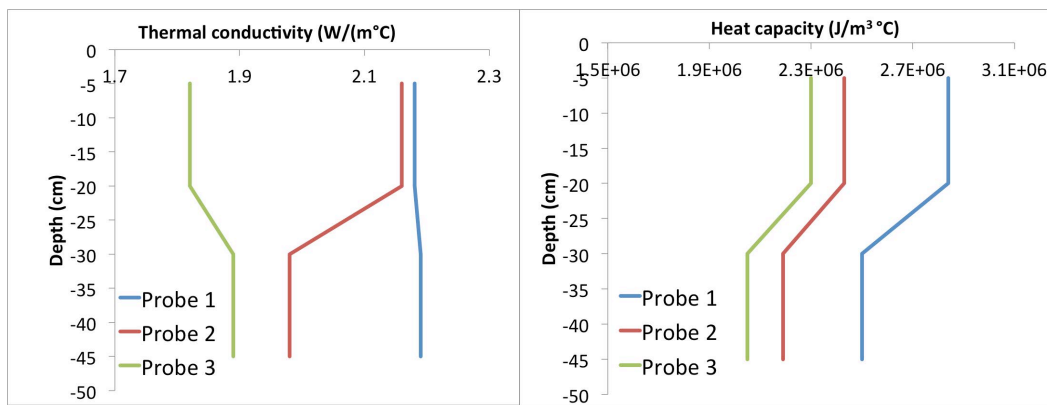


Figure 3.26: Thermal conductivity and heat capacity tests of saturated sediment samples from the temperature probe locations.

Relatively lower thermal conductivity and heat capacity measurements for the saturated sediment samples from the probe 3 location (Figure 3.26) are consistent with electromagnetics, self-potential, and laboratory resistivity results that indicate coarser sediment textures with less clay content in the north of the infiltration pond. The development of the clogging layer is apparent in the heat capacity measurements of sediment samples (Figure 3.26), where heat capacity of the near-surface sediments within the clogging layer is greater due to increased fines accumulated within pore spaces.

1DTempPro models were parameterized with the thermal conductivity and heat capacity measurements and were calibrated by adjusting specific discharge to best match the temperature data. An example of the first 1DTempPro model for probe 1 data (from 6–20cm depth) is plotted below (Figure 3.27).

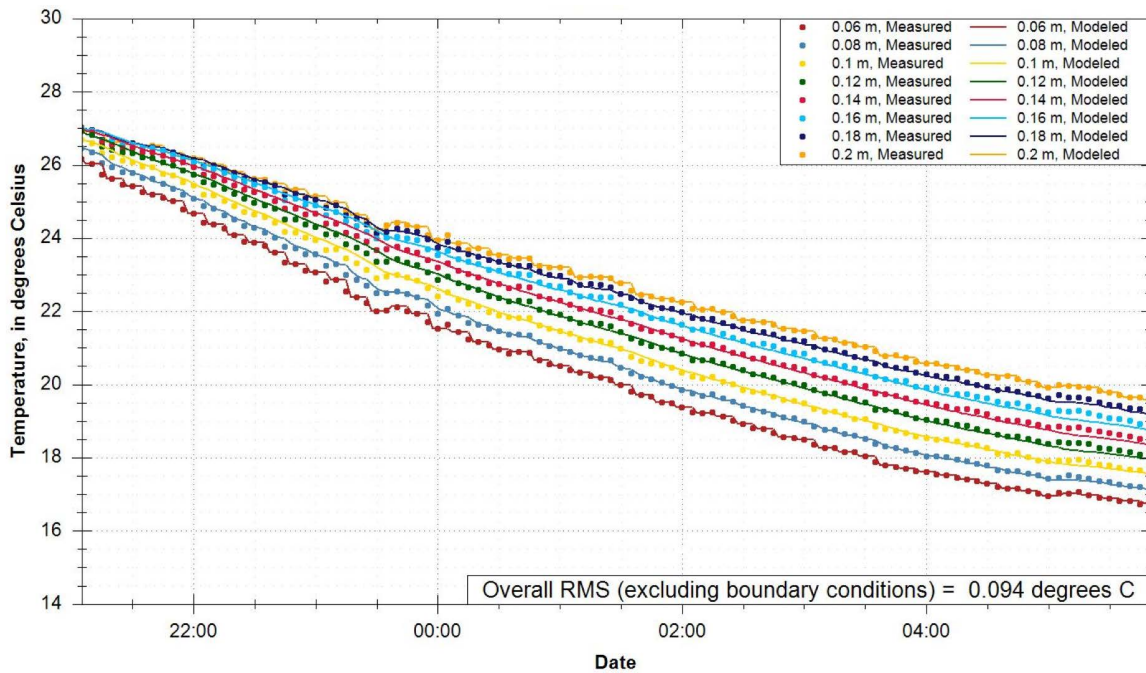


Figure 3.27: 1DTempPro model of probe 1 data (with 10 minute temporal resolution) from 6–20 cm depth with 0.02 m vertical resolution in the modeled and measured temperature time series of the first day of basin flooding. The overall RMS value (0.094 °C) suggests very well constrained modeled temperature changes with depth compared to measured temperature changes.

The high-resolution temperature sensing data in Figure 3.27 depicts a measured and modeled downward propagating cold front due to cold groundwater advection, dispersion, and conduction. For the sake of simplicity, modeling maintained constant porosity (0.377) and constant dispersivity (0.1 m) for all models because changes less than 1 order of magnitude to specific discharge estimations could only be achieved when porosity or dispersivity were adjusted by 1 or more magnitudes, which may be unrealistic. Head changes are not included in the modeling because the increase in height

of surface water due to flooding and ponding was less than 5 cm basin-wide during the modeled measurement period, which should have a negligible contribution to hydraulic forcing and groundwater flow velocity. Specific discharge estimates from 1DTempPro models suggest very low specific discharge at the probe 1 and probe 2 locations (Figure 3.28).

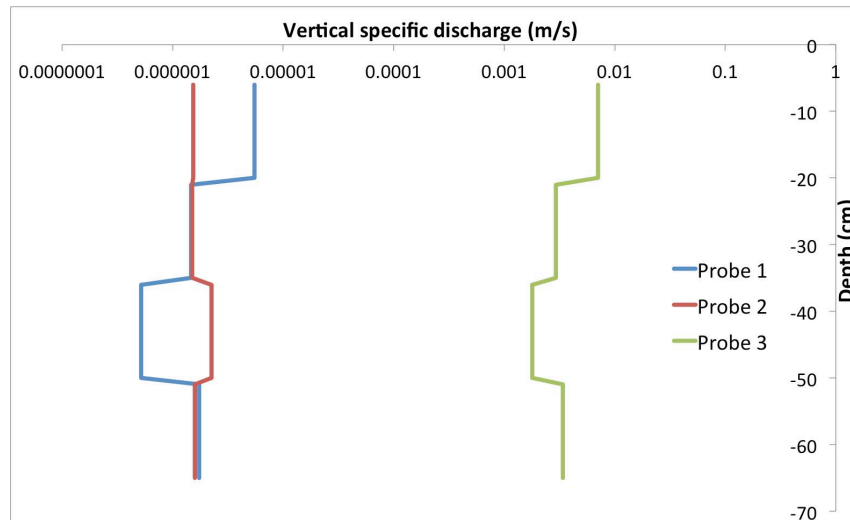


Figure 3.28: Specific discharge estimates from 1DTempPro models of high-resolution temperature sensing data along probes 1, 2, and 3 with depth.

Very low specific discharge values are estimated within the simulated (14 cm thick) homogeneous layers from probe 1 and 2 data modeling (Figure 3.28). Temperature signals associated with cold groundwater advection are lost by about 68 cm depth during the measurement period due to heat attenuation. The low probe 1 and 2 discharge estimates (Figure 3.28) are consistent with the low maximum recovery well pumping rates south of the infiltration pond (Figure 3.25) as well as the underwater self-potential results that suggest lower permeability and porewater velocities near the ground surface in the south of the infiltration pond. Electromagnetics and laboratory resistivity tests also suggest finer sediment textures with lower permeability in the southern area of the infiltration pond. Probe 3 data modeling produced estimates of specific discharge that are

three orders of magnitude greater than probes 1 and 2 (Figure 3.28). Higher specific discharge estimates from probe 3 are consistent with the relatively lower underwater self-potential anomalies in the north of the infiltration pond that suggest increased streaming current contributions associated with higher near-surface specific discharge rates and coarser, more permeable, sediment textures.

3.3 Electrical resistivity tomography

An electrical resistivity tomography survey was conducted with an ABEM Terrameter unit, 5 m spacing between electrodes, and Wenner geometry during recovery well pumping and pond drainage with partially saturated conditions at the ground surface within the infiltration pond and along the berm (Figure 3.30).



Figure 3.30: Electrical resistivity tomography survey location (red line) with the steady recovery well pumping rates (in GPM) during the measurement period.

The electrical resistivity tomography survey provided useful spatial information of electrical resistivity distributions with depth. The electrical resistivity tomogram allows

us to qualitatively infer features such differences in sediment textures, saturation, and clay content at depth. The electrical resistivity tomography survey imaged the shale bedrock at about 20 m depth (Figure 3.31), which is consistent with well log data.

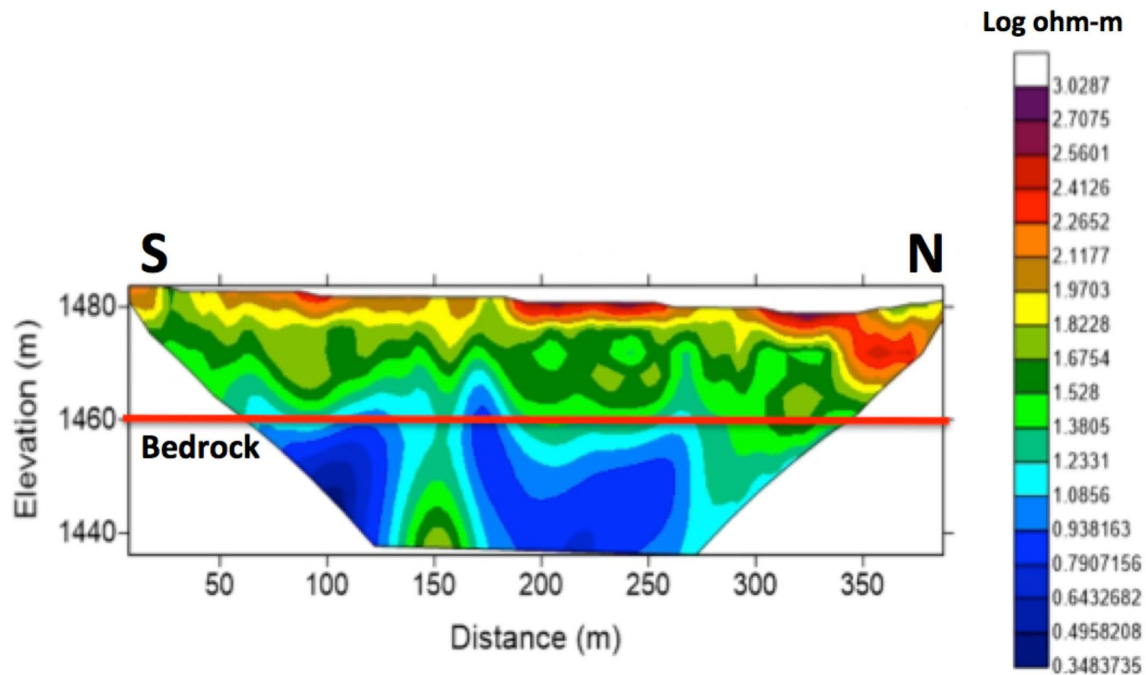


Figure 3.31: Electrical resistivity tomogram. More resistive anomalies toward the north (N) are associated with increased drainage and lower saturation within coarser sediment textures. Less resistive anomalies near the ground surface toward the south (S) are associated with increased saturation and finer sediment textures. The water table is interpolated to be ≈ 5 m below the ground surface.

Interpolations of permeability and sediment textures from electrical resistivity tomography anomalies (Figure 3.31) are made with the assumption that clay content and saturation decreases the electrical resistance of a medium (Tyler *et al.*, 2009). Low resistance at ≈ 20 m depth is interpolated as the shale bedrock (Figure 3.31), which was previously observed during recovery well construction at the Aurora ARR site.

3.4 Electromagnetics

An electromagnetics survey was conducted with a Geonics EM-31 unit to estimate the electrical conductivity of sediments at a 3 m half-depth in the infiltration pond during saturated conditions with no recovery well pumping (Figure 3.40).

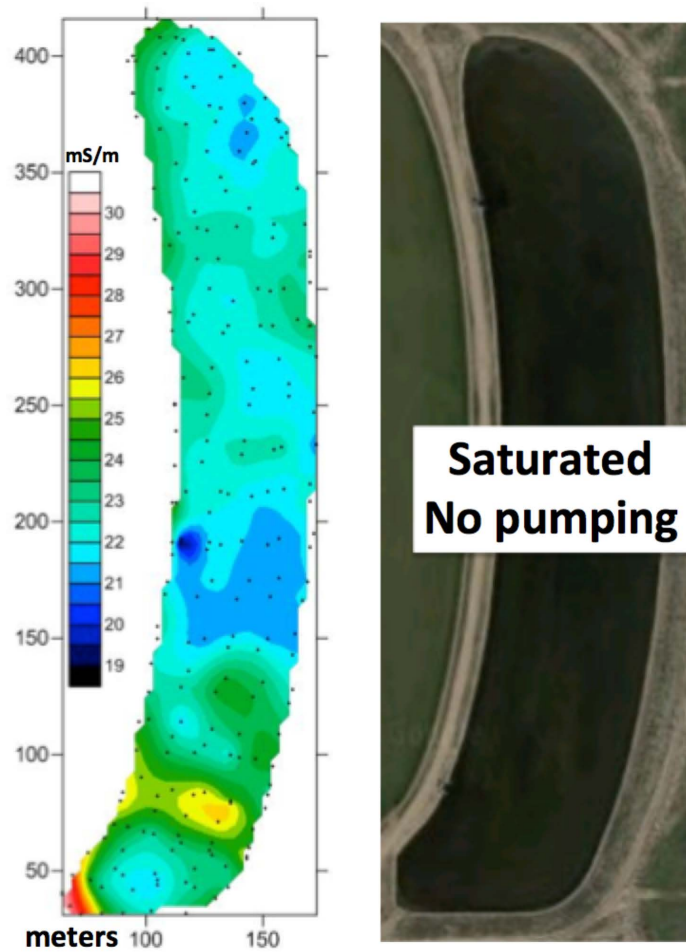


Figure 3.40: Electromagnetics (EM-31) survey results (dots are measurement points recorded with a GPS in UTM coordinates).

Low electrical conductivity anomalies in the electromagnetics survey are interpolated to be associated with coarser sediment textures with less clay content within the central and northern areas of the infiltration pond (Figure 3.40). High electrical conductivity anomalies are interpolated to be associated with increased clay content in the southern area of the infiltration pond (Figure 3.40), which is consistent with observations from

underwater self-potential, high-resolution temperature sensing results, and pumping well rates that are associated with restricted infiltration in the southern area of the infiltration pond.

3.5 Laboratory electrical resistivity tests

Sediment samples were collected from the eastern central infiltration pond in a large grid, with 10 samples taken from within the clogging layer ($\approx 10\text{--}20$ cm) and 10 samples taken from the lower native sediments ($\approx 30\text{--}40$ cm). A method for low frequency (1, 10, and 100 Hz) resistivity tests of these samples with an impedance spectrometer system in a laboratory was developed. A protocol was established for drying the sediment samples and then slowly saturating them by dripping $1010\ \mu\text{S}/\text{cm}$ water (similar to the observed floodwater electrical conductivity) within a vacuum chamber (with constant -0.07 MPa pressure) and letting them sit for 24 hours to equilibrate. Although pebbles larger than 1 cm diameter are removed from each sediment sample to minimize error, larger grains are less likely to polarize at low frequencies (1, 10, and 100 Hz), where fines predominantly affect the bulk electrical conductivity of saturated media (Revil *et al.*, 2012).

The average geometrical factor for the glass container and electrode array setup (with 2 cm spacing between ABMN electrodes) was determined by averaging resistivity measurements (at 1, 10, and 100 Hz frequencies) within three batches of water with known electrical conductivities (420, 1048, and 2082 $\mu\text{S}/\text{cm}$ respectively). The known electrical conductivities of water batches are converted to resistivity (in ohm-m), where the geometrical factor equals the known water resistivity (in ohm-m) divided by the

measured absolute resistivity (in ohm) of each water sample. The geometrical factor for the experimental setup was estimated to be 0.115 m (which is well constrained with a mean squared error of 0.012 m) based on 9 absolute resistivity measurements (in ohm) within the 3 different water samples of known resistivity (in ohm-m) measured separately with an electrical conductivity meter. Estimations of apparent resistivity (in ohm-m) of the saturated sediment samples are obtained by averaging the measured absolute resistivity values (in ohm) at 1, 10, and 100 Hz frequencies and then multiplying by the geometrical factor. The experimental setup for the 4-electrode array (1 mm diameter steel electrodes) and the sediment container utilized for analysis with the impedance spectrometer is shown below (Figure 3.50).

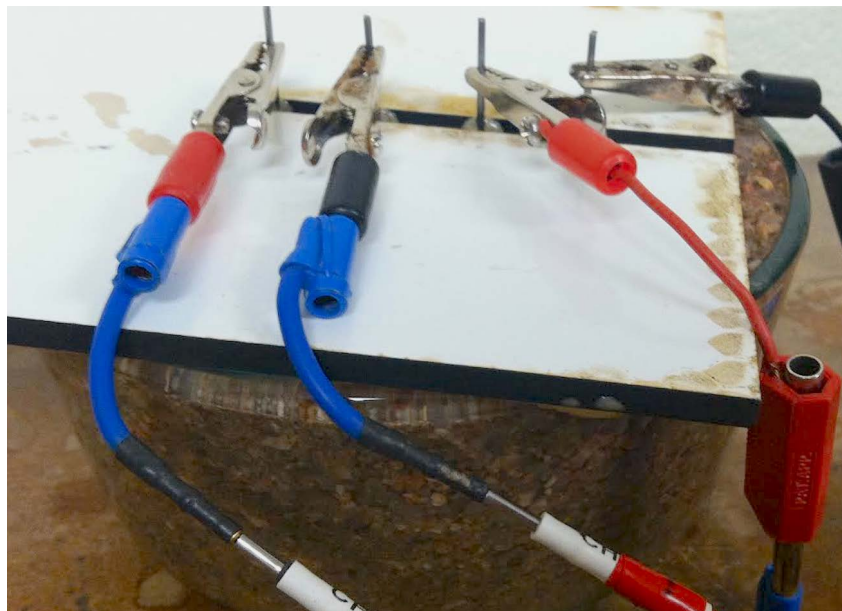


Figure 3.50: Experimental setup for laboratory resistivity tests of sediment samples with the impedance spectrometer system with 4 (1 mm diameter) steel electrodes and 2 cm spacing.

Although results from laboratory resistivity tests provide consistent estimations of resistivity (in ohm-m), the layering and ordering of grain sizes within sediment samples from the field were destroyed during the experiment protocol, which requires breaking up

the dried sediments prior to the vacuum saturation method. This results in the mixing of fine organic and inorganic materials throughout the sediments samples, where fines may have been originally organized in more ordered layers prior to mixing and packing into the glass container.

Apparent resistivity estimations of sediments samples with the impedance spectrometer system still provide useful spatial information about sediment textures within the clogging layer and lower native sediments in the eastern central infiltration pond. The laboratory electrical resistivity test method allows for more controlled porewater conductivities, saturation, and temperature for each sediment sample, thereby increasing the contribution to electrical conductivity from the fines content. Apparent resistivity estimations (in ohm-m) are inverted to electrical conductivity values (in mS/m) to provide two electrical conductivity maps of the clogging layer (10–20 cm depth samples) and the lower native sediments (30–40 cm depth samples) (Figure 3.51).

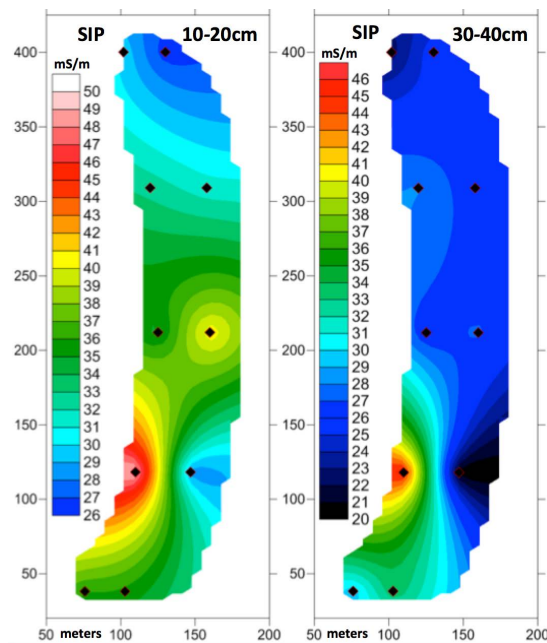


Figure 3.51: Electrical conductivity maps of laboratory resistivity test results of the clogging layer (left 10–20 cm) and the lower native sediments (right 30–40 cm) plotted with SURFER11 for spherical Kriging between sampling points (dots).

The electrical conductivity maps provided by the laboratory resistivity tests (Figure 3.51) indicates higher electrical conductivities within the clogging layer (10–20 cm depth samples) throughout the eastern central infiltration pond. Greater electrical conductivity values throughout the clogging layer basin-wide (Figure 3.51) is indicative of the net accumulation of fines within surface sediments. Differences in surface water stability may induce spatial variance in algae growth, accumulation and clogging layer development processes throughout the infiltration pond. Low electrical conductivity measurements of clogging layer sediments in the north of the infiltration pond is consistent with high specific discharge estimates from the high-resolution temperature sensing probe 3 location associated with coarser sediment textures and less accumulation of fines. This is also consistent with the lower heat capacity measurements from the probe 3 location. The high electrical conductivity anomaly within the 30–40 cm depth samples in the southern area of the infiltration pond (Figure 3.51) is indicative of greater fines content within the lower native sediments, which is consistent with high-resolution temperature sensing, underwater self-potential, and electromagnetics results that indicate lower permeability, finer sediment textures and lower discharge in the southern area of the eastern central infiltration pond.

3.6 Numerical modeling

Finite element forward modeling is conducted with COMSOL Multiphysics in order to synthesize geophysical information, estimate permeability, and best match observed underwater self-potential anomalies. We utilize underwater self-potential measurements along an east-west transect in the center of the eastern central infiltration

pond in line with the eastern pumping well to construct a 2D cross section. Minimum underwater self-potential values are observed on the eastern side and maximum values on the western side with a relative difference of about 10 mV in both underwater self-potential surveys #1 and #2 (Figure 3.60).

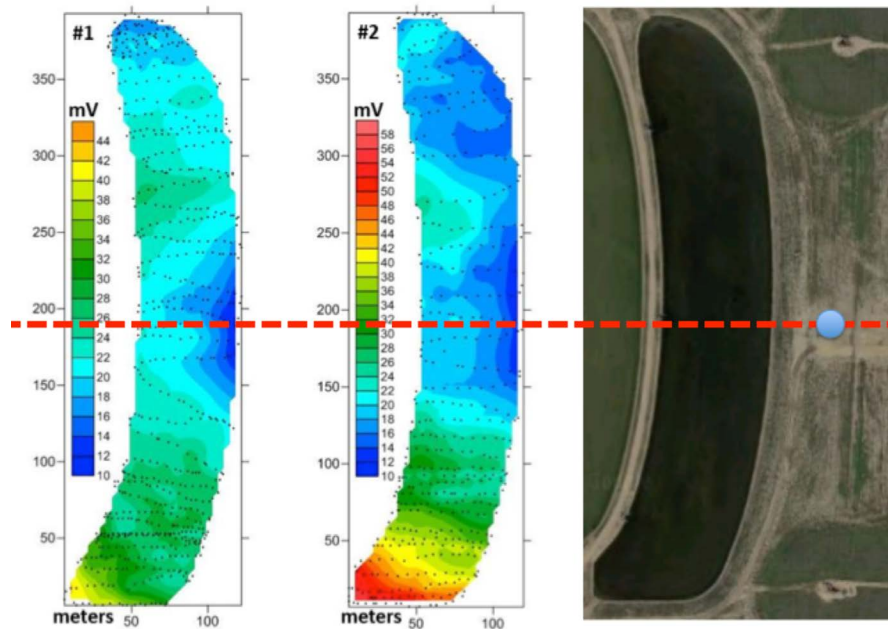


Figure 3.60: Simulated 2D vertical cross section location (red dashed line) over underwater self-potential surveys #1 and #2. The relative difference of measured self-potential values along the simulation transect is 10 mV.

In the COMSOL simulation, we adjust the pumping rate of the eastern recovery well in order to better match the relative 10 mV self-potential differences along the 2D transect because we only know the true pumping rate in the 3D case. A homogeneous permeability parameter for the simulated unconfined layer is based on the temperature sensing estimates of specific discharge from probe 3 in the north of the infiltration pond, which could be associated with the similar range of self-potential and electrical conductivity measurements in the central and northern areas of the infiltration pond. The 2D finite element domain is fully saturated with the infiltration pond assigned as a constant head boundary and all the other surrounding boundaries assigned as no flux and

zero background self-potential. Under the steady state groundwater flow simulation, all the infiltrated water is pumped out of the eastern recovery well at a rate of 70 GPM

(Figure 3.61).

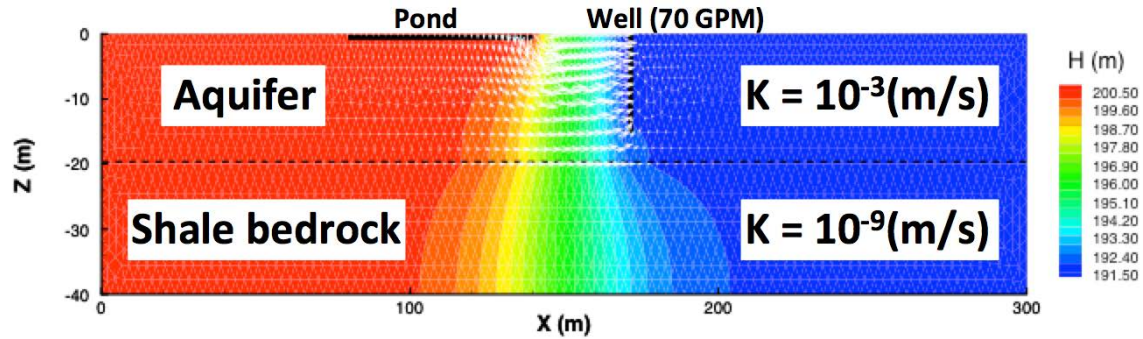


Figure 3.61: 2D COMSOL steady state groundwater flow simulation head distribution and groundwater velocity vector distribution. The outer edges of the domain are parameterized as zero flux boundaries based on the low permeability slurry wall, which produces relatively lower simulated pressure and head towards the right.

After the Darcy equation is solved for within the finite element space in the steady state simulation (Figure 3.61), the estimated groundwater velocity values (\mathbf{u}) are applied to the coupled continuity equation for electrical charge as follows:

$$\nabla \cdot (\sigma \nabla \varphi) = \nabla \cdot (\hat{Q}_V \mathbf{u}) \quad [15]$$

where the electrical conductivity term (σ) is assigned as a constant (0.02 S/m) within the upper aquifer based on electromagnetics results and the bedrock is assigned as (0.1 S/m) based on electrical resistivity results (Figure 3.62).

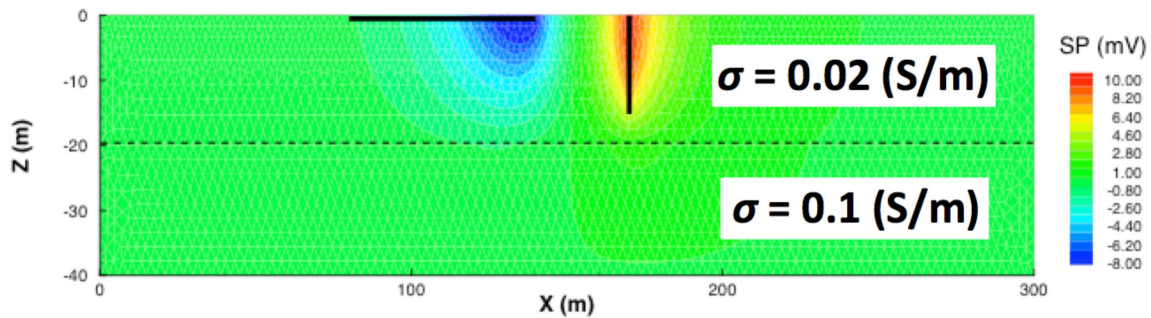


Figure 3.62: 2D COMSOL self-potential simulation based on groundwater velocity, permeability, and electrical conductivity distributions.

The simulated 10 mV relative self-potential difference between the eastern side and western side of the pond (Figure 3.62) is matched to the observed relative drop of 10 mV in underwater self-potential measurements along the transect (Figure 3.60). Although the 2D COMSOL simulation highly simplifies the self-potential phenomena measured in the field, streaming current contributions to self-potential signals consistently become relatively more negative towards the eastern boundary within the pond due to increased proximity to the eastern recovery well, increased hydraulic forcing, and infiltration. In the 3D forward modeling case, observed pumping well rates from the field can be simulated with layered electrical conductivity distributions from the combination of geophysical methods and near-surface permeability distributions calibrated within the known temperature sensing constraints in order to best match the observed relative self-potential anomalies.

3.7 Conclusions

The measured underwater self-potential signals were sensitive to differences in groundwater flow and permeability indicative of variable clogging layer development throughout the eastern central infiltration pond. Geophysical results showed greater fines content, lower permeability and discharge within the southern area of the infiltration pond, which is associated with risks of increased surface water stability, algae growth, clogging layer development, anoxic conditions, and decreased hydraulic loading rates. 3D forward modeling allows for the synthesis of geophysical information for permeability mapping, which is important for effective aquifer recharge and recovery system design and optimization strategy development.

REFERENCES CITED

- Bouwer, H., Rice, R. C., 1989, Effect of water depth in groundwater recharge basins on infiltration. *J. Irrig. Drain Eng.*, 115, 556-567.
- Ma, L., Spalding, R. F., 1997, Effects of artificial recharge and recovery on ground water quality and aquifer storage recovery. *Journal of the American Water Resources Association*, 33, 3.
- Ikard, S. J., Revil, A., Jardani, A., Woodruff, W. F., Parekh, M., Mooney, M., 2012, Saline pulse test monitoring with the self-potential method to nonintrusively determine the velocity of the pore water in leaking areas of earth dams and embankments. *Water Resources Research*, 48, W04201.
- Briggs, M., Lautz, L., McKenzie, J., Gordon, R., Hare, D., 2012, Using high-resolution distributed temperature sensing to quantify spatial and temporal variability in vertical hyporheic flux. *Water Resour. Res.*, 48, W02527.
- Revil, A., Karaoulis, M., Johnson, T., Kemna, A., 2012, Review: Some low-frequency electrical methods for subsurface characterization and monitoring in hydrogeology. *Hydrogeology Journal*, 20, 617-658.
- Morris, E. R., 2009, Height-above-ground effects on penetration depth and response of electromagnetic induction soil conductivity meters. *Computers and Electronics in Agriculture*, 68, 150-156.
- Zimmermann, E., Kemna, A., Berwix, J., Glaas, W., Münch, H. M., Huisman, J. A., 2008, A high-accuracy impedance spectrometer for measuring sediments with low polarizability. *Meas. Sci. Technol*, 19, 105603.
- Hering, J. G., Waite, T. D., Luthy, R. G., Drewes, J. E., Sedlak, D. L., 2013, A Changing Framework for Urban Water Systems. *Environmental Science and Technology*, Special Issue: Design Options for More Sustainable Urban Water Environment.
- Yoon, M. K., Drewes, J. E., Amy, G. L., 2013, Fate of bulk and trace organics during a simulated aquifer recharge and recovery (ARR)-ozone hybrid process. *Chemosphere*, 93, 2055-2062.
- Hübner, U., Miehe, U., Jekel, M., 2012, Optimized removal of dissolved organic carbon and trace contaminants during combined ozonation and artificial groundwater recharge. *Water Research*, 46, 6059-6068.

Drewes, J. E., Quanrud, D. M., Amy, G. L., Westerhoff, P. K., 2006, Character of organic matter in Soil-Aquifer treatment systems. *Journal of Environmental Engineering*, 132, 1447-1458.

Smedley, P. L., Kinniburgh, D. G., 2002, A review of the source behavior and distribution of arsenic in natural waters. *Applied Geochemistry*, 17, 517-568.

Jardani, A., Revil, A., Barrash, W., Crespy, A., Rizzo, E., Straface, S., Cardiff, M., Malama, B., Miller, C., Johnson, T., 2009, Reconstruction of the Water Table for Self-Potential Data: A Bayesian Approach. *Ground Water*, 47, 2, 213-277.

Revil, A., Jardani, A., 2010, Stochastic inversion of permeability and dispersivities from time lapse self-potential measurements: A controlled sandbox study. *Geophysical Research Letters*, 37, L11404.

Jardani, A., Revil, A., Bolève, A., Crespy, A., Dupont, J. P., Barrash, W., Malama, B., 2007, Tomography of the Darcy velocity from self-potential measurements. *Geophysical Research Letters*, 34, L24403.

Ahmed, A. S., Jardani, A., Revil, A., Dupont, J. P., 2013, SP2DINV: A 2D forward and inverse code for streaming potential problems. *Computers & Geosciences*, 59, 9-16.

Jardani, A., Revil, A., Santos, F., Fauchard, C., 2007, Detection of preferential infiltration pathways in sinkholes using joint inversion of self-potential and EM-34 conductivity data. *Geophysical Prospecting*, 55, 749-760.

Mary P. Anderson, 2005, Heat as a Groundwater Tracer. *Ground Water*, 43, 6.

Tyler, W., Selker, J., Hausner, M., Hatch, C., Torgersen, T., Thodal, C., Schladow, S., 2009, Environmental temperature sensing using Raman spectra DTS fiber-optic methods. *Water Resour. Res.*, 45, W00D23.

Selker, J., Thévenez, L., Huwald, H., Mallet, A., Luxemburg, W., Giesen, N., Stejskal, M., Zeman, J., Westhoff, M., Parlange, M., 2006, Distributed fiber-optic temperature sensing for hydrologic systems. *Water Resources Research*, 42, W12202.

Healy, R. W., 1990, Simulation of solute transport in variably saturated media with supplemental information on modifications to the U.S. Geological Survey's computer program VS2D: U.S. Geological Survey Water-Resources Investigations Report 90-4025, 125.

Healy, R. W., Ronan, A. D., 1996, Documentation of computer program VS2DH for simulation of energy transport in variably saturated porous media – modification on the U.S. Geological Survey's computer program VS2DT: U.S. Geological Survey Water-Resources Investigations Report 96-4230.

Voytek, E. B., Drenkelfuss, A., Day-Lewis, F. D., Healy, R., Lane, Jr. J. W., Werkema, D., 2013, 1DTempPro: Analyzing Temperature Profiles for Groundwater/Surface-water Exchange. Submitted to Ground Water.

Constantz, J. 2008. Heat as a tracer to determine streambed water exchanges, *Water Resources Research*, 44, 4, W00D10.

Vogt, T., Schneider, P., Hahn-Woernle, L., Cirpka, O. A. 2010. Estimation of seepage rates in a losing stream by means of fiber-optic high-resolution vertical temperature profiling. *Journal of Hydrology*, 380, 154-164.

Clément, R., Descloitres, M., Günther, T., Ribolzi, O., Legchenko, A., 2009, Influence of shallow infiltration on time-lapse ERT: Experience of advanced interpretation. *Geoscience*, 341, 886-898.

Oldenborger, G., Knoll, M., Routh, P., LaBrecque, D., 2007, Time-lapse ERT monitoring of an injection/withdrawal experiment in a shallow unconfined aquifer. *Geophysics*, 72, 4, F177-F187.

Miller, C., Routh, P., Brosten, T., McNamara, J., 2008, Application of time-lapse ERT imaging to watershed characterization. *Geophysics*, 73, 3, G7-G17.

Daily, W., Ramirez, A., LaBrecque, D., Nitao, J., 1992, Electrical Resistivity Tomography of Vadose Water Movement. *Water Resources Research*, 28, 5, 1429-1422.

Santi, P. M., Crenshaw, B. A., 2003, Demonstration projects using wick drains to stabilize landslides. *Environmental & Engineering Geoscience*, 9, 4, 339-350.

Graham, N. J. D., 1999, Removal of humic substances by oxidation/biofiltration processes, a review. *Water Science and Technology*, 40, 141-148.